Title
Multiferroic Devices for Cell Manipulation and Acoustic Resonators

Author
Zheng, Ruoda

Publication Date
2023

Peer reviewed|Thesis/dissertation

UNIVERSITY OF CALIFORNIA

Los Angeles

Multiferroic Devices for Cell Manipulation and Acoustic Resonators

A dissertation submitted in partial satisfaction of the
requirements for the degree Doctor of Philosophy
in Mechanical Engineering

by

Ruoda Zheng

2023

ABSTRACT OF THE DISSERTATION

Multiferroic Devices for Cell Manipulation and Acoustic Resonators

by

Ruoda Zheng

Doctor of Philosophy in Mechanical Engineering

University of California, Los Angeles, 2023

Professor Gregory P. Carman, Chair

Microscale magnetic devices have garnered significant attention due to their non-volatility, which is the result of energy stored in the spinning of electrons. The key to operating magnetic devices is to control the magnetization, and among all the mechanisms, the strain-mediated multiferroics approach is particularly energy efficient. This approach uses a piezoelectric-magnetoelastic heterostructure, where an input voltage is applied on a piezoelectric thin film to actuate an acoustic response. This film is coupled with magnetostrictive elements, so the induced strain reorients the magnetization vector. This reorientation is currently widely used for storing information like in memory applications. In this dissertation, it will be explored for other applications such as controlling magnetic beads for cell manipulation and producing an electromagnetic signal as an acoustically actuated antenna.

Chapter 1 introduces the concept of multiferroics and the theoretical foundations required for analysis and design. Techniques will be presented for both simulation and fabrication aspects.

Several published papers on relevant topics will be reviewed. These works indicate that the multiferroics approach has great potential for achieving energy efficiency and miniaturization.

Chapter 2 focuses on the magnetic device's use in a cell manipulation application. A design for a magnetically activated cell sorting device is proposed, and the analytical and experimental work involved is described in detail. A multiphysics finite element model was built in order to estimate the time-dependent magnetic forces and the movement trajectory of the cells. This model was used to design the device after verifying its accuracy against experimental values. Three different designs are investigated: (1) a single magnet for cell manipulation, (2) a single magnet for individual cell manipulation, and (3) an array of magnets for individual cell manipulation. The final array design is able to individually control each magnet to individually capture or release a single cell as required for time-dependent post processing.

Chapter 3 focuses on the use of multiferroics in an acoustically actuated antenna application. A design is proposed and all analytical and experimental work involved is described in detail. The device is based on magnetoelectric coupling and operates at acoustic resonance in a standing shear bulk wave mode. The methodology for combining the device's micromagnetic, solid mechanics, and electromagnetic behavior is discussed. Multiphysics models are built in order to estimate the mechanical and magnetization response in both transmission and reception modes for the proposed design. The radiation of the magnetic material, the piezoelectric substrate, and the parasitic effects of the wires are investigated. The fabricated device successfully demonstrates mechanical resonance and magnetoelectric coupling. The results show the device's potential for miniaturization and its promise for future compact antenna design.

Finally, Chapter 4 summarizes the contents and the main results of the dissertation.

The dissertation of Ruoda Zheng is approved.

Yuanxun Wang

Dino Di Carlo

Robert N. Candler

Abdon Eduardo Sepulveda

Gregory P. Carman, Committee Chair

University of California, Los Angeles

2023

To my family

Table of Contents

List of Figures

List of Tables

VITA

Education:

2018-2020 M.S. in Mechanical Engineering
University of California, Los Angeles

2014-2018 B.S. in Aircraft Design
Beijing University of Aeronautics and Astronautics, Beijing, China

Employment History:

2018-2022 Graduate Student Researcher
Translational Applications of Nanoscale Multiferroic Systems (TANMS)

Publications:

[1] Victor Estrada, **Ruoda Zheng**, Yilian Wang, Hiromi Miwa, Michael Bogumil, Dino Di Carlo, Greg Carman, Abdon Sepulveda, "Arrayed Single Cell Capture and Release using Localized Oersted Fields", submitted to Adv. Mater. Technol. (2023)

[2] **Ruoda Zheng**, Victor Estrada, Jin-Zhao Hu, Nishanth Virushabadoss, Rashaunda Henderson, Greg Carman, Abdon Sepulveda. "A Lamb Wave Magnetoelectric Antenna for Implantable Devices", to be submitted to Appl. Phys. Lett. (2023)

[3] **Ruoda Zheng**, Jin-Zhao Hu, Qianchang Wang, Victor Estrada, Abdon E. Sepulveda. "Breaking the Symmetry for Magnetic Reorientation with Perpendicular Magnetic Anisotropy", submitted to IEEE Journal on Multiscale and Multiphysics Computational Techniques. (2023)

[4] Zhuyun Xiao, Chelsea Lai, **Ruoda Zheng**, Maite Goiriena-Goikoetxea, Nobumichi Tamura, Cornelio Torres Juarez, Colin Perry, Hanuman Singh, Jeffrey Bokor, Gregory P. Carman, and Rob N. Candler, "Localized strain profile in surface electrode array for programmable composite multiferroic devices", Appl. Phys. Lett., vol. 118, no. 18, 2021. (2021)

Conference Presentations:

[1] **Ruoda Zheng**, Victor Estrada, Gregory P. Carman, Abdon E. Sepulveda, "Multiferroic Lamb Wave Antenna", at Conference on Magnetism and Magnetic Materials, Oral presentation. (2021).

[2] **Ruoda Zheng**, Victor Estrada, Abdon Sepulveda. "Dynamic Simulation of Micromagnetic Beads Separation", at SIAM CSE mini-symposium, Invited talk. (2021).

[3] **Ruoda Zheng**, Victor Estrada, Gregory P. Carman, Abdon E. Sepulveda, "Multiferroic Lamb Wave Antenna with Energy Reflecting Components", In Conference on Magnetism and Magnetic Materials, Oral presentation. (2020).

[4] Victor Estrada, **Ruoda Zheng**, Gregory P. Carman, Abdon E. Sepulveda, "Magnetically Activated Cell Capture and Release using Spin-Orbit Torque", at Conference on Magnetism and Magnetic Materials. (2019).

Chapter 1. Introduction

1.1 Multiferroics

One of the major challenges in the development of magnetic devices is the ability to switch the magnetization. Several current-based methods have been studied, such as the Oersted field, current-induced spin transfer torque (STT), and spin-orbit torque (SOT). [1]–[11] An alternative voltage-based method, known as the strain-mediated multiferroic approach, has gained increasing attention in recent years. [12]–[21] This mechanism employs a ferromagnetic-ferroelectric heterostructure to achieve highly energy-efficient switching. In this chapter, despite the backgrounds and motivations of specific magnetic device applications, we will focus on the multiferroic mechanism.

Traditionally, multiferroics refer to materials that exhibit two or more primary ferroic couplings, including ferromagnetism, ferroelectricity, and ferroelasticity. However, few materials possess both ferromagnetic and ferroelectric properties at the same time. BiFeO3, or BFO, is one such material that has an intrinsic magnetoelectric effect at room temperature. However, its weak net magnetization due to the Dzyaloshinskii-Moriya Interaction (DMI) limits its practical applications. [22] As a result, the definition of multiferroics has been expanded to include magnetoelectric (ME) coupling, in which electrics and magnetics can be translated through the strain at the ferromagnetic-ferroelectric heterostructure interface.

The coupling between electrics, magnetics, and mechanics is illustrated in Figure 1-1 to help understand the relationship. It should be noted that, according to the strict definition, multiferroic is not equivalent to magnetoelectricity.

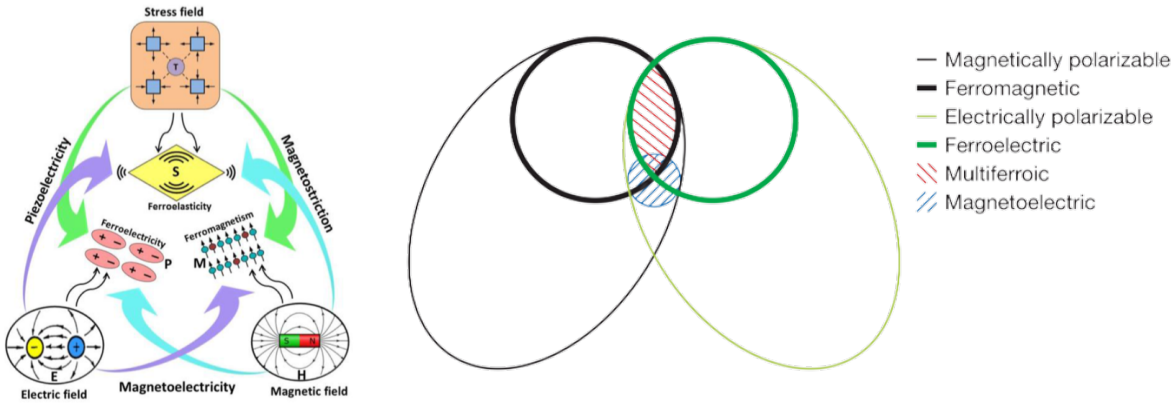

Figure 1-1: (a) Coupling between mechanics, electrics, and magnetics. (b) Relationship between multiferroic and magnetoelectric materials, reference [19], [23].

Researchers have extensively studied the electric-field control of magnetism in various mechanically-coupled composite multiferroic heterostructures, where strain from a piezoelectric material influences magnetism in an adjacent magnetoelastic material due to the converse magnetoelectric effect. [10], [20], [21], [24] In typical ferromagnetic-ferroelectric heterostructures, as shown in Figure 1-2, an input voltage is applied to the piezoelectric thin film to produce an acoustic response. [25]–[30] This film is coupled with magnetostrictive elements, and the resulting strain reorients the magnetization. One well-known magnetostrictive material is Terfenol-D, which consists of TbFe2 and DyFe2 and has a high saturation magnetostriction of 2400 ppm at room temperature.

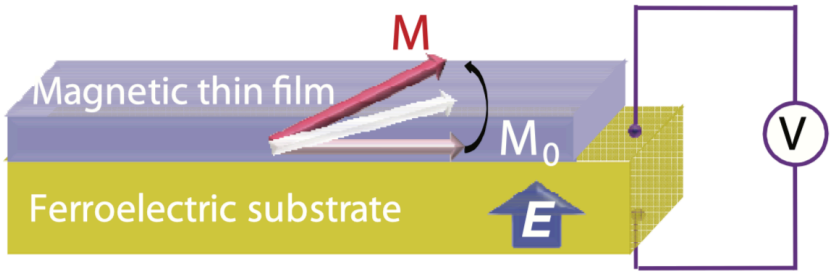

Figure 1-2: A typical ferromagnetic–ferroelectric heterostructure, reference [24].

Strain-mediated magnetization switching has been widely studied in memory applications [31][32]. Later, Bootsmann et al. [33] used pure tensile stress to switch the magnetization of Co micromagnets to a new in-plane easy axis perpendicular to the stress. Reversible switching of Ni thin films was then achieved on both PZT thin film and PMN-PT substrates. In 2013, Cui proposed the use of island electrodes to individually switch magnets on PZT, as PZT can generate bi-axial strain with opposite directions, inducing strong magnetoelastic anisotropy. In 2014, Liang et al. [34][35] implemented the weak form of the Landau-Lifshitz-Gilbert equation into finite element analysis to build a fully coupled model for multiferroic magnetization simulation. The setup is as follows.

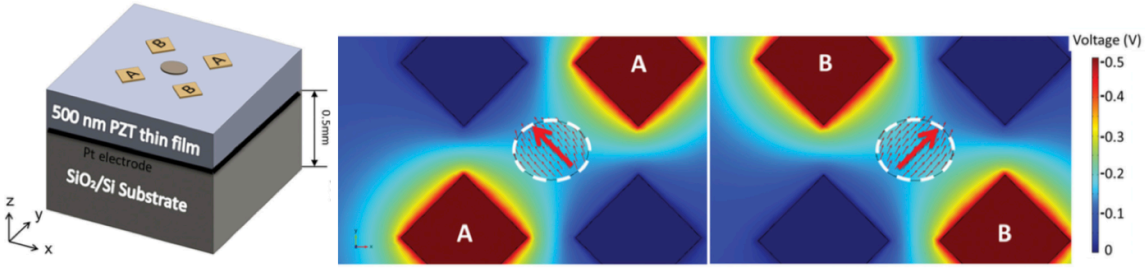

Figure 1-3: A fully coupled model for strain-mediated magnetization switching in a multiferroic heterostructure, reference [34].

In summary, the use of voltage-generated strain to control magnetism in miniaturized devices is an energy-efficient alternative to the conventional current-driven approach because it reduces Joule heating. These devices are based on a class of materials known as multiferroics. Recent advances in room-temperature magnetoelectric composites have brought us closer to realizing a wide range of energy-efficient technological applications [36][23] based on fundamental research discoveries. There has been significant progress in developing more compact, faster strain-mediated magnetoelectric coupling-based applications, particularly in data-storage devices [37][38] such as straintronic [39] magnetoelectric random-access memory (MeRAM) [37] and probabilistic computing platforms. Other applications, such as radio-frequency (RF) / microwave devices [40][41] and microfluidic particle / cell sorting platforms [42][43], will be discussed in future work.

1.2 Methods

The precessional magnetization dynamics of the single domain magnetoelastic dot are governed by the Landau-Lifshitz-Gilbert (LLG) equation:

$$\frac{\partial \mathbf{m}}{\partial t} = -\mu_0 \gamma (\mathbf{m} \times \mathbf{H}_{\text{eff}}) + \alpha_{\text{G}} \left(\mathbf{m} \times \frac{\partial \mathbf{m}}{\partial t} \right) \qquad \text{Eq. } 1-1$$

where $\mathbf{m}$ is the normalized magnetization, μ_0 is the vacuum permittivity, γ is the gyromagnetic ratio, $\mathbf{H}_{\text{eff}}$ is the effective magnetic field, and α_{G} is the Gilbert damping parameter. The first term on the right-hand side represents precessional torque accounting for the gyromagnetic motion,

while the second term represents damping of the precessional motion. The effective magnetic field can be obtained from the total energy density and is given by:

$$\mathbf{H}_{\mathrm{eff}} = -\frac{1}{\mu_0 M_s}\frac{\partial \mathrm{E}_{\mathrm{tot}}}{\partial \mathbf{m}} = \mathbf{H}_{\mathrm{ext}} + \mathbf{H}_{\mathrm{ex}} + \mathbf{H}_{\mathrm{anis}} + \mathbf{H}_{\mathrm{d}} + \mathbf{H}_{\mathrm{me}}(\mathbf{m}, \boldsymbol{\varepsilon}) \qquad \mathrm{Eq.}\, 1-2$$

where $\mathrm{E}_{\mathrm{tot}}$ is the total energy density, $\mathbf{H}_{\mathrm{ext}}$ is the applied external magnetic field, $\mathbf{H}_{\mathrm{ex}}$ is the effective exchange field, $\mathbf{H}_{\mathrm{anis}}$ is the effective anisotropy field, $\mathbf{H}_{\mathrm{d}}$ is the effective demagnetization field, and $\mathbf{H}_{\mathrm{me}}(\mathbf{m}, \boldsymbol{\varepsilon})$ is the effective magnetoelastic field.

The precession can also be regarded as the process towards the minimization of the total free energy density [44], which is written as follows:

$$\mathrm{E}_{\mathrm{total}} = E_{ext} + E_{ex} + E_{anis} + E_d + E_{el} \qquad \mathrm{Eq.}\, 1-3$$

Each energy density term corresponds to a field term above.

The external energy density E_{ext} is associated with an applied external magnetic field. It is minimized when the magnetization is parallel with the external field and maximized when antiparallel. It is written in index notation i, j as:

$$E_{ext} = -\mu_0 M_s m_i H_i^{ext} \qquad \mathrm{Eq.}\, 1-4$$

The exchange energy density E_{ex} is associated with the magnetization gradient. This term is expressed in terms of the exchange stiffness constant A_{ex} as:

$$E_{ex} = A_{ex} m_{i,j} m_{i,j} \qquad \mathrm{Eq.}\, 1-5$$

The anisotropic energy density E_{anis} is associated with lattice structures and preferred directions of magnetization. It is expressed in terms of the magnetic crystal anisotropy constants $K_1,\ K_2$:

$$E_{anis} = K_1(m_1^2m_2^2 + m_2^2m_3^2 + m_3^2m_1^2) + K_2(m_1^2m_2^2m_3^2) \qquad \text{Eq. } 1-6$$

The demagnetization energy density E_d is associated with effective demagnetization field as:

$$E_d = -\frac{1}{2}\mu_0 M_i H_i^d \qquad \text{Eq. } 1-7$$

The elastic energy density E_{el} is associated with elastic strains and expressed as:

$$E_{el} = \frac{1}{2}c_{ijkl}\left(\varepsilon_{ij} - \varepsilon_{ij}^m\right)\left(\varepsilon_{kl} - \varepsilon_{kl}^m\right) \qquad \text{Eq. } 1-8$$

where ε_{ij} is the total strain, ε_{ij}^m is the magnetoelastic strain. For amorphous materials, the magnetoelastic strains are given by with the saturation magnetostriction λ_s:

$$\varepsilon_{ij}^m = 1.5\lambda_s\left(m_i m_j - \frac{1}{3}\right), \quad i = j \qquad \text{Eq. } 1-9$$

$$\varepsilon_{ij}^m = 1.5\lambda_s m_i m_j, \quad i \neq j \qquad \text{Eq. } 1-10$$

The above system of equations is written in weak form and implemented into a finite element software. Magnetics and mechanics are coupled. The backward differentiation formula is used for implicit equations. A segregated solver is used, which keeps iterating until the error is below the tolerance, and the result converges.

1.3 Experimental Techniques

1) Lithography

Lithography is the primary process used to transfer patterns from a mask to a photoresist. This photoresist can then be used for either deposition or etching. The lithography process includes several steps: spin coating, exposure, baking, development, and stripping. The resolution of the lithography process is proportional to the wavelength of the light source used. State-of-the-art deep UV light sources have wavelengths as low as 193 nm. In our case, we use ultraviolet (UV) photolithography with a minimum feature size of approximately 3 μm.

The photoresist can be either positive or negative, depending on its polarity. The choice of resist is determined by the design and resolution of the mask. Negative resist is generally more physically robust and compatible with the lift-off process due to the undercut effect. However, in some cases, such as large-area etching, using a dark mask and negative resist can make alignment difficult. In our case, we use nLOF 2020 or AZ 5214 for different layers.

We also encountered a problem with the sparking of the piezoelectric substrate during baking. Abrupt increases in temperature can reorient the polarization and induce electrical redistribution. In the worst case, the thermal discharge can damage the entire substrate. We learned that we should always ramp up the temperature slowly for piezoelectric substrates, even though this requires recalibrating the baking time.

2) Thin film deposition

We mainly used two deposition techniques: electron beam evaporation and sputtering. In the cell manipulation project, all films were deposited and patterned using electron beam evaporation and the lift-off process. This technique involves directing an electron beam at the target material, causing it to heat up and evaporate. The resulting vapor is then coated on the substrate in a directional manner. In the acoustic resonator project, the magnetic thin film was deposited using sputtering. In this technique, charged ions in the plasma bombard the target, causing atoms to be knocked off. This non-directional diffusion typically results in a conformal and dense film.

3) Etching

We mainly used two etching techniques: wet etching and dry etching. Cavities in Si in the acoustic resonator project were created using wet etching. This technique is based on a chemical reaction and is isotropic. Vias through AlN in the acoustic resonator project were created using dry etching, specifically reactive ion etching. This technique uses charged ions in the plasma to react with the thin film, resulting in a directional etching process with relatively high accuracy. Dry etching is non-directional and typically results in a conformal and dense film.

4) Magnetic characterization

We mainly used two magnetic characterization techniques: SQUID and VSM. A superconducting quantum interference device (SQUID) is a sensitive magnetometer used to measure the magnetization-magnetic field (M-H) hysteresis loop. It is based on superconducting loops containing Josephson junctions. A vibrating sample magnetometer (VSM) is another technique used to characterize magnetic properties. It is based on the induced voltage in a pickup coil next

to a vibrating sample under an alternating magnetic field. It is worth noting that the magneto-optic Kerr effect (MOKE) can be used to measure time-dependent magnetic moments, but this was not required in our projects. The direction of magnetization is characterized using magnetic force microscopy (MFM), which is based on atomic force microscopy (AFM) with a magnetic coating on the tip. A vibrating tip is brought near the magnetic sample, and a laser spot and photodiode detector are used to detect the phase change in the cantilever motion due to the magnetic force. The scanning of the x-y plane maps the magnetization over the thin film.

5) Piezoelectric characterization

The polarization-electric field (P-E) hysteresis loop is measured using a Sawyer-Tower circuit tool. This tool is based on the change in voltage on a shunt capacitor connected to the sample under an alternating electric field. The definitions of the coercivity electric field, saturation polarization, and remanent polarization are the same as in magnetics. The induced strain can be measured using a traditional strain gauge or X-ray microdiffraction. The strain gauge is a simple way to measure strains above 100 ppm. X-ray microdiffraction has higher sensitivity and can map the elastic strain distribution at the microscale. Pre-polarization is crucial for testing, as an unpolarized sample will give varying strain values.

6) Radiofrequency testing

Commercialized tools such as a vector network analyzer (VNA), E-field probe, H-field probe, ground signal ground (GSG) probe, and printed circuit board (PCB) are used in RF testing. Most tests are performed on a probe station platform in a non-shielded environment.

Chapter 2. Cell Manipulation

2.1 Introduction

Immunotherapy, a technique used in cancer treatment, has gained significant attention in recent years. [45] This therapy involves extracting immune cells from a cancer patient's body, modifying them at the cellular level, and reintroducing them into the patient to target and attack cancerous growths. To make this possible, specific types of immune cells must be isolated from the extracted blood of the patients. This process is known as cell sorting. One cell sorting technique is magnetically activated cell sorting (MACS), which uses magnetic force to attract immune cells tagged with magnetic beads. [46] Current MACS technology has high throughput [47], but typically lacks the ability to precisely manipulate cells. Single-cell accuracy is crucial as the behavior of a single cell may differ significantly from that of the surrounding population. In addition, MACS cannot conduct time-dependent analyses. To address these limitations, we propose a new micromagnetic cell sorting design that has the advantage of large arrays of individually addressable elements and the ability to conduct long-term on-chip studies. Experimental results have shown the feasibility of this design.

2.1.1 Motivation

Cell sorting has become an essential technique in various biological and biomedical applications due to developments in fields such as personalized medicine and advancements in cancer treatments. The most commonly used cell sorting methods in today's market are Magnetically

Activated Cell Sorting (MACS) and Fluorescence-Activated Cell Sorting (FACS). MACS relies on the principle of magnetic attraction to sort cells tagged with magnetic beads. It is widely used in industry due to its high throughput, high selectivity, and ease of use. However, its accuracy is relatively low, and cell damage can occur during the mechanical release process. FACS employs a similar mechanism, but cells are tagged with fluorescent proteins instead of magnetic beads. [48] The fluorescent signal is used to polarize droplets individually, and an electric field is then used to manipulate the droplets. Single-cell sorting accuracy can be achieved, but this technique requires an optical system and another cell collection platform. [49] Neither method offers high throughput, high accuracy, and long-term analysis capabilities simultaneously, which makes using these techniques for actual therapy processes time-consuming and costly. Therefore, more modern cell sorting techniques that address these issues are needed.

One potential alternative method is to perform MACS on a microfluidic chip platform and combine it with an optical system capable of single-cell identification and manipulation. This would involve using micromagnets to capture magnetically tagged cells in a microfluidic channel and then controlling the magnetization to release single cells based on their fluorescent signatures. This device would combine the benefits of both MACS and FACS.

The idea of reducing the size of MACS systems is not new. Microfluidic devices have many advantages, such as high throughput, low cost, and the ability to conduct fast low-volume experiments. These devices also allow for electronic control of the capture and release of magnetic cells, which is not possible with traditional MACS systems that use bulk permanent magnets. By

changing the magnetization direction of micromagnets, the magnetic forces on cells can be tuned and their motion controlled. As a result, micromagnets are a promising method for cell manipulation.

2.1.2 Literature review

1) Current cell sorting techniques

Although conventional cell sorting methods, including centrifugation and chemical methods, have been widely used in industry and show high sorting efficiency, they are mostly expensive, time-consuming, and unsuitable for processing small-volume blood samples [50]. The following literature review will present state-of-the-art microfluidic cell sorting techniques and discuss each method's advantages and disadvantages. Microfluidics-based sorting devices that exploit various physical principles have been proven to offer similar capabilities, with the advantages of miniaturized sizes, high sensitivity, and increased portability [51].

Current microfluidic cell sorting techniques are generally classified as active or passive. Active implies that microfluidic devices rely on an external field while passive implies that they rely predominantly on the inherent cell properties [52]. Both classifications have their advantages and disadvantages. Ideally, a perfect method should be able to perform single-cell sorting rapidly and efficiently. However, this has not yet been demonstrated. We have chosen MACS as a candidate to achieve these goals due to its high throughput, low cost, and successful usage in nanoscale computer memory applications.

a) Active cell sorting techniques

Magnetically activated cell sorting (MACS)

Magnetically activated cell sorting (MACS) is a common active cell sorting technique. As the name suggests, MACS operates on the principle of magnetic attraction of desired cells. The cells are made magnetic by tagging them with tiny superparamagnetic (SPM) beads that have been functionalized with antibodies that will attach only to specific surface makers on the desired cells. The cell mixture then flows through a channel, and an external magnetic field displaces the magnetically tagged cells and captures them indefinitely. The researcher can then remove the permanent magnets and release the tagged cells. The advantages of MACS include high throughput and relatively low cost. Notably, another fabulous advantage is that the magnetic field is predominantly permeable to biological tissues and less likely to interfere with cell function or immunochemistry necessary for magnetic labeling, thereby minimizing any physical damage to the cells [53]. However, low sensitivity (difficulty capturing cells in subpopulations below 1% [54]) is an apparent shortcoming for MACS. Shown below are examples of devices that operate using MACS principles. These devices include mechanisms where permanent magnets are placed outside and inside the channel. Additionally, an example of cell sorting using intrinsically magnetic cells (red blood cells) is illustrated.

MACS with internal magnets

Although external permanent magnets are portable and convenient, embedding micromagnets within the channel [46] can provide higher magnetic flux gradients. Figure 2-2 demonstrates a

recent device containing NdFeB magnet arrays. With a vertical magnetic field, magnets can immobilize and guide the self-assembly of magnetic beads conjugated with antibodies. Moreover, the analysis using actual patients' samples agrees with the flow tests, indicating its utility as a cheap and fast diagnostic system [55].

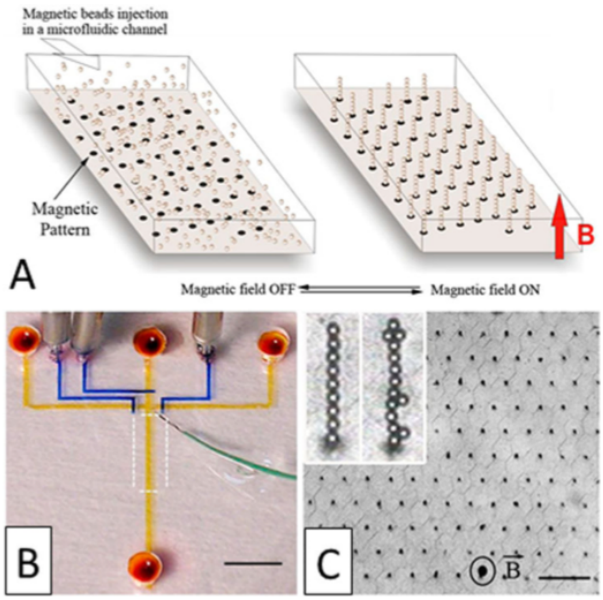

Figure 2-1: Magnetically activated cell sorting (MACS) with embedding micromagnets, reference [46].

MACS with external magnets

In Figure 2-1, part A, permanent magnets are placed underneath the main microfluidic channel [56]. Here magnets with opposite magnetization are placed side by side to enhance the magnetic flux gradient. Circulating tumor cells (CTC) tagged with magnetic beads will be attracted toward the bottom, while other untagged blood cells will go with laminar flow and exit through the outlet. In experiments, microcavity arrays are on the bottom to collect the CTCs. Cells can then be

released after sorting by moving magnets away. Part B shows a sophisticated microfluidic system that integrates inertial and MACS selection. Initially, red blood cells (RBC) are depleted through hydrodynamic sorting due to their light mass. Then CTCs with magnetic beads are routed up under magnetic fields, and unwanted diamagnetic white blood cells (WBC) are depleted at the same time [57].

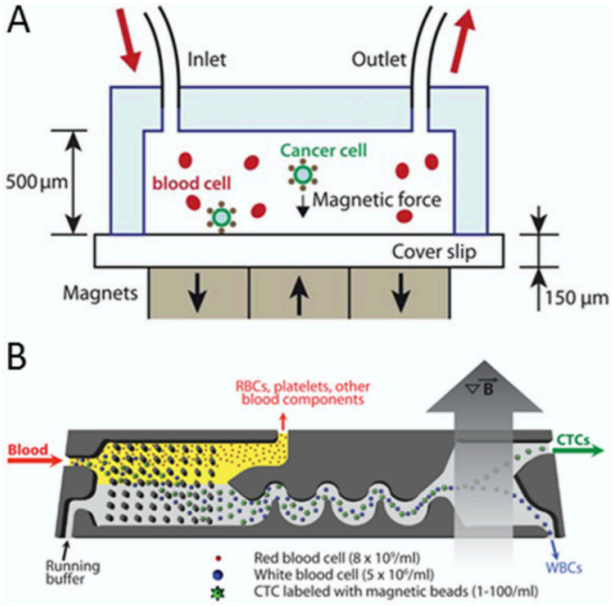

Figure 2-2: Magnetically activated cell sorting (MACS) with external magnets, reference [56] [57].

Apart from MACS with magnetic labels, the inherent magnetic properties of cells can also be utilized to separate them. For example, RBCs are paramagnetic, while WBCs are diamagnetic. Current techniques can isolate 90% of RBCs and WBCs into two collection outlets with a ferromagnetic wire and an external field of 0.2 T [58]. But the efficiency is limited by the cells' weak susceptibility, which also hampers all similar label-free sorting techniques.

Placing magnets within the channel is the most effective method for achieving rapid single-cell sorting amongst all MACS configurations. This is due to the high magnetic field gradients generated with such structures and the potential for these devices to be miniaturized to single-cell scales.

Fluorescence-activated cell sorting (FACS)

Fluorescence-activated cell sorting (FACS) is another common active cell separation technique. In this method, fluorophores functionalized with antibodies will specifically attach to surface markers of desired cells within a heterogeneous mixture, essentially making these cells fluorescent. An optical detector then analyzes the mixture of cells. If a fluorescent label is detected, a tangential electric field or optical pressure is applied to change the fluorescent cell's path into a collection channel. FACS has exceptionally high sensitivity and mature engineering development. Although FACS traditionally exhibits low throughput, higher throughput (10000/s) [59] is possible considering the commercialization of parallel microfluidic cytometer systems. Therefore, FACS is regarded as a benchmark in cell sorting techniques. However, the main shortcoming is its high equipment expense and maintenance cost.

In one experiment setup of a FACS device [49], first, cells are focused into a single line by sheath flow. In the detection region, the optical tweezer displaces cells into one of two outlets based on the presence or absence of fluorescent labels. The fluorescence images show a significant difference in cell populations between waste and collection outlets, thus indicating high selectivity.

Then, conventional droplet-based FACS is illustrated. Cells encapsulated in liquid droplets are sorted individually, indicating high sensitivity [60].

Electrokinetic cell sorting is a similar technique to FACS. It uses a laser to inspect and identify cells with fluorescent labels. It then switches the trajectory of these cells to predetermined paths. In figure 2-3, on the left, charged electrodes control the migration of solvated ions, which alters the direction of flow [61]. On the right, air bubbles generated by electrodes control the T-switch mechanically, which manipulates the flow direction [62]. Sometimes a cell's intrinsic electric properties can also be utilized to achieve sorting. However, these properties are often too insignificant to be effectively implemented.

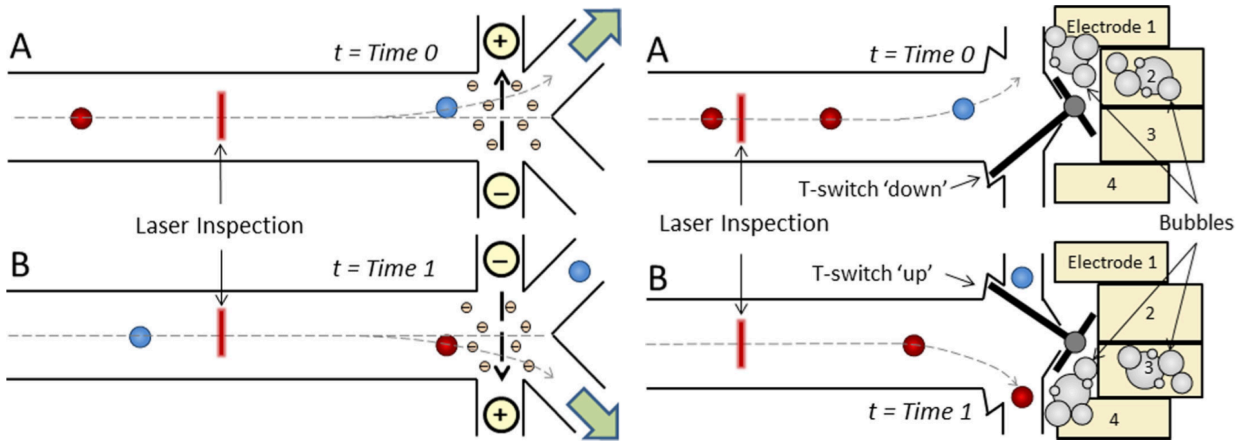

Figure 2-3: Fluorescence-activated cell sorting (FACS) and Electro kinetic cell sorting schematic illustrating the working principle, reference [61][62].

It is essential to notice that, in the electrokinetic process, the actual cell identification is made by a FACS system. The optical mechanism tells the T-switch what type of cells are being analyzed,

and they should be displaced. This device enables researchers to obtain more information about heterogenous cell populations than a MACS system.

The acoustofluidic cell sorting [63] is another proper supplementary technique to MACS or FACS systems. In this system, Interdigitated transducers (IDTs) create an acoustic standing wave on the surface of the channel. Cells are focused along defined streamlines depending on the driving frequencies. Like inertial cell sorting, which enriches CTCs based on density before sorting them out in Figure 2-1, acoustofluidic manipulation can serve as a precursor to focus cells before another sorting procedure. These precursors help eliminate undesired items in the channel and increase the accuracy and throughput of the primary cell sorter.

b) Passive cell sorting techniques

Size-dependent sorting is a passive cell sorting technique. In this mechanism, small cells fall into smaller cavities, whereas more giant cells are prevented from doing so due to their size. These more giant cells are then captured in larger cavities. In a mass-dependent sorting [64], cells reach an equilibrium state under shear and wall effect forces at a certain height so they can be sorted by different inertial lift forces.

The critical point in this design is that the system utilizes the channel's geometry and can be easily integrated with other existing microfluidic cell sorting mechanisms. Similar to acoustofluidic devices, this type of mechanism can be an addition to MACS or FACS protocols.

2) Magnetization switching by an external field

Conventional MACS systems use only external magnets to separate cells into a giant collective outlet. After micromagnets were implemented into microfluidics, cells with magnetic beads could be captured by micromagnets inside the channel. Using this technology, researchers began investigating the possibility of manipulating cells, including capturing/moving/releasing them by changing the magnetization of micromagnets [43].

Using external fields is still the most popular method of magnetization switching. These methods include turning on/off an external magnetic field, turning on/off current to control an electromagnet, and simply bringing/taking away a permanent magnet to control the magnetization of micromagnets inside a microfluidic channel.

External magnetic field

Marco Donolato et al. [65] simulated the injection and propagation of a domain wall in a snake-like structure. Later they experimentally demonstrated that a magnetic bead would move with the domain wall (from the left to right side) under the action of external magnetic fields (up or down). The device worked like a stepper motor and successfully manipulated a magnetic bead in the microscale using domain wall motion in the external field [33], [66]–[68].

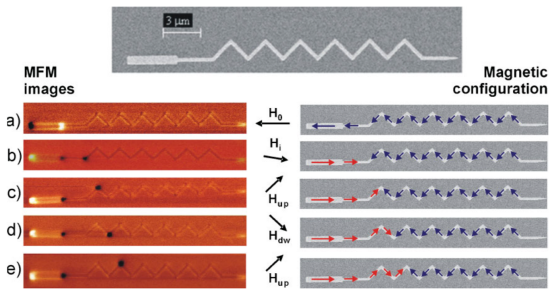

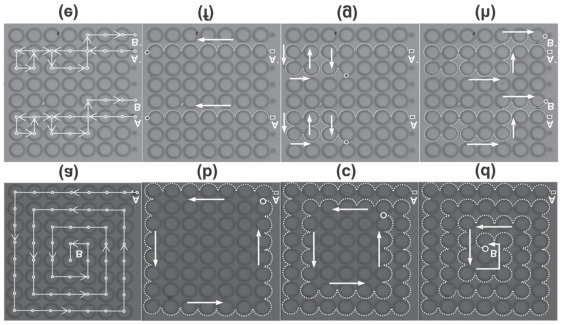

Figure 2-4: Beads manipulation by external magnetic field induced domain wall motion, reference [65].

In 2014, Anandakumar Sarella et al. [69] improved the device to achieve more arbitrary motion. They used a ring to take the place of the linear track. They could rotate a bead on the disk with a domain wall by rotating the external field. They could move the bead from one ring to another by introducing an external magnetic field pulse. In Figure 2-4, a ring array was built. A bead was first captured at point A. Controlling the field, it moved along a pre-defined pathway and reached destination B. This experiment showed the capability of micromagnets to perform programmable manipulation of a single magnetic bead.

External permanent magnet

In 2017, Coleman Murray et al. fabricated a magnetic ratcheting system. [70] The system included permanent magnets on a rotating motor generating a cycling magnetic field and a micromagnet array with increasing distance. The rotating permanent magnets change the magnetization of the micromagnet array on the chip. This cyclic change of magnetization will attract beads and move them from one micromagnet site to the next. However, If the micromagnets are placed too far from

each other, they will not be able to achieve this motion. That distance is defined as the critical pitch. Because beads with higher magnetic content have larger essential pitches, they can thus be separated from beads with less content. This mechanism implements a novel design that combines macro mechanical motion with magnetization in microfluidics.

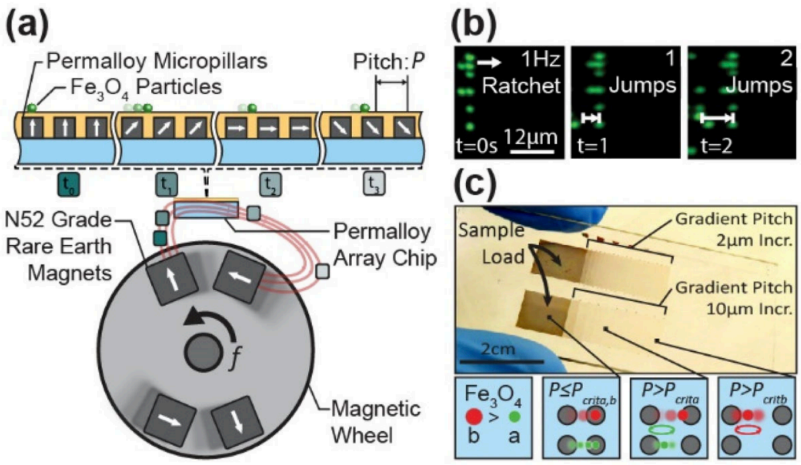

Figure 2-5: Beads manipulation by external magnetic ratcheting, reference [70].

Electromagnet

The similar idea is to use electromagnet-controlled permanent magnets to move magnetic liquid droplets, as shown in Figure 2-6. [71][72] An electromagnet array is built at the bottom. The permanent magnet is on top of the circuit and underneath the channel. By turning on/off adjacent current, the magnet will jump from one spot to the next, carrying the droplet. Electric current flowing in such small structures can make Joule heating an issue for such systems. It is also important to note that a permanent magnet is necessary here to amplify the magnetic flux created by the coils.

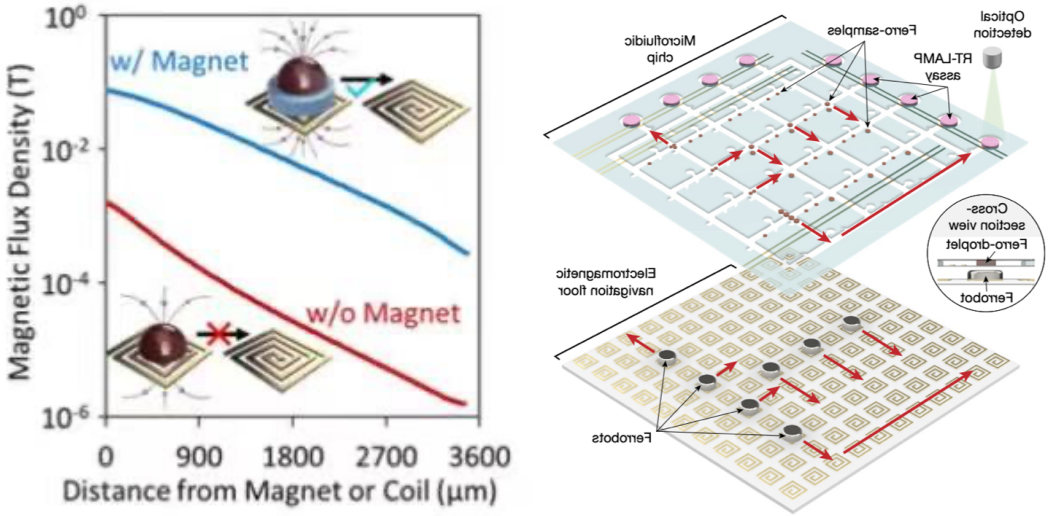

Figure 2-6: Beads manipulation by embedding electromagnets, reference [71][72].

In the field of memory, Niemier et al. used on-chip Cu wires to generate a local magnetic field instead of an external field in 2007. [73] They experimentally demonstrated that local nanomagnets could be switched using an Oersted field, as in Figure 2-7. It looks like a simple version of a single magnet switching, but it can't be transferred to the micro-scale because the energy is not large enough.

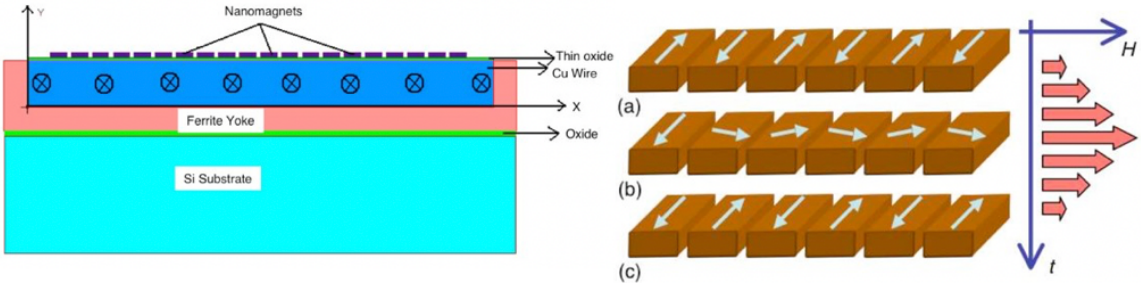

Figure 2-7: Magnetization switching by embedding metal wires, reference [73].

External fields to control magnetization appear robust enough in the cell sorting field. However, as researchers went smaller and smaller in scale, the shortcomings of using external fields appeared. Its effective range is usually large enough to switch multiple micromagnets simultaneously but cannot be small enough to manipulate a single cell [69]. Even in work that claimed to realize single-cell manipulation, they could not control more than one cell independently. Alternatively, if we use micro-electromagnets that can be easily turned off individually, they can barely provide enough force to capture magnetic beads. In other words, all external switching methods, including external magnetic fields, micro-size electromagnets, and magnets motion, are almost fundamentally limited in scale, being unsuitable for performing single-cell manipulation. A new mechanism that can individually switch a micromagnet is needed.

4) Magnetization switching by strain

Strain-mediated switching is another mechanism that can achieve single micromagnet control. It is a more energy-efficient and more localized way to control magnetization.

In the field of cell sorting, switching through strain is not as expected, but there are still some

pioneering works. In 2015, Hyunmin Sohn et al. [74] simulated and fabricated a composite multiferroic heterostructure consisting of a ferromagnetic Ni ring on the Pt-coated surface of a PMN-PT substrate. The magnetization switching was observed under XMCD-PEEM and successfully induced magnetic bead motion. However, the release was poorly controlled due to residual strain in the piezoelectric film. In 2017 [75], they improved it by using multiple island electrodes with a PZT substrate. A complete rotation cycle is observed below:

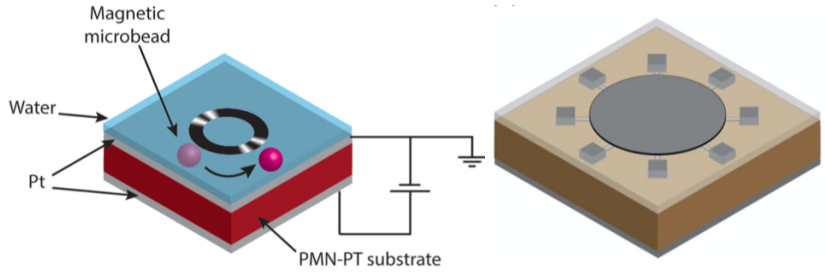

Figure 2-8: Single-step and multi-step magnetization rotation by voltage-induced strain, reference [75].

Based on these devices, Xiao et al. [43] ran a microfluid experiment with fluorescent-labeled magnetic beads and captured the beads on the north and south poles of micromagnets. But again, the structure could hardly release the beads since its magnetization does not go back when the voltage is turned off. [76]

In addition to in-plane switching, perpendicular magnetic anisotropy (PMA) is also utilized in memory [1], [77]–[80] and cell sorting. Yu-ching et al. [42] showed PMA capture in 2019. Up to this stage, it has not been proven to have a significant benefit over in-plane switching other than its magnetic stability due to a higher energy barrier.

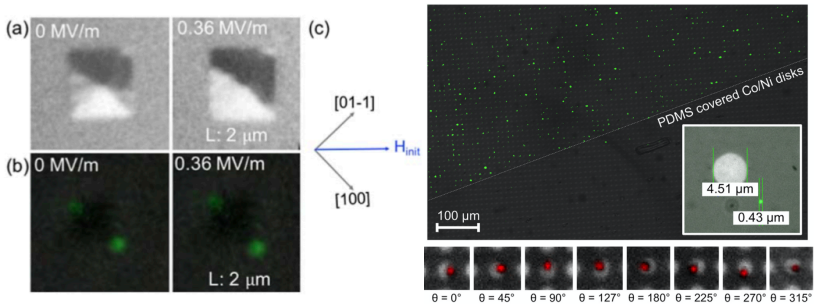

Figure 2-9: Magnetic beads captured in-plane or out-of-plane under fluorescent view, reference [42].

The feasibility and developments of strain-mediated magnetization switching are discussed above. [43] Although energy dissipation of joule heating might not be a critical issue in cell sorting if the current is only on during the switching process, it can still be super beneficial to the design of the MACS system.

5) Magnetization switching by SOT

Spin-orbit torque (SOT) switching is one mechanism that can achieve single micromagnet control. SOT consists of injecting an electric current into a heavy metal layer in contact with a ferromagnetic layer. Electrons in the wire transfer orbital angular momentum to electrons in the magnet, consequently changing the magnetization. The feasibility of this method has been experimentally shown in multiple structures and materials Fields [81]–[86].

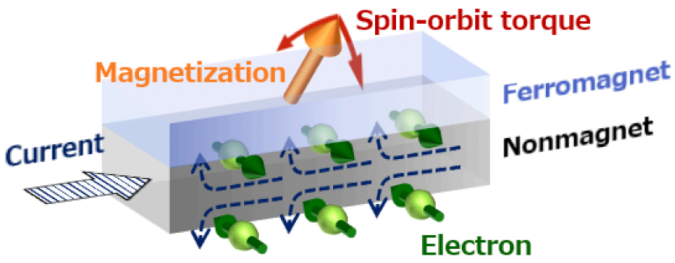

Figure 2-10: SOT schematic illustrating the working principle, reference [80].

Spin-orbit torque is generated from a combination of a crystalline structure lacking inversion symmetry and spin-orbit coupling. When an unpolarized current flows through the wire, electrons with spins of opposite polarities accumulate at the opposing surfaces because of the spin hall effect. After that, two effects contribute to the generation of torque. On the one hand, because of sp-d

orbits exchange coupling, top electrons in the wire can transfer angular momentum to bottom electrons in the magnet. This interfacial effect is Rashba torque. It is also called a field-like torque since the effect is equivalent to an induction magnetic field. On the other hand, the redistribution of electrons introduces a lateral structural symmetry in the device and gives rise to a torque on more electrons in the bulk magnet. It is also called spin hall torque since it acts like a damping precession.

2.2 Proposed design

The device we propose here is an original cell sorting design conceived using state-of-the-art mems and microfluidics technology. The final device's geometry consists of an array of rectangular magnetic structures deposited under a microfluidic channel, as shown in Figure 2-9. Each magnet is able to capture or release a single cell and be individually controlled.

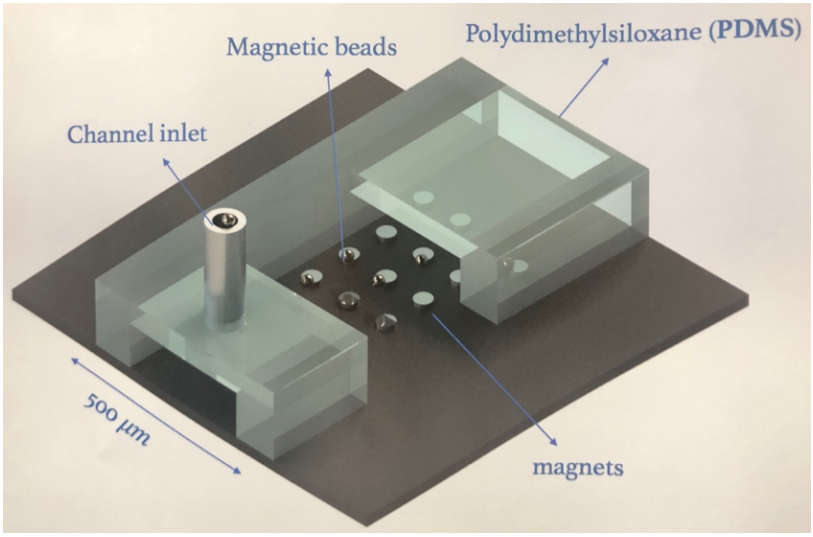

Figure 2-11: The device consists of a PDMS channel and Si substrate with an array of magnets.

2.2.1 A single magnet for cell manipulation

We started with a single magnet that can capture and release many beads. The proposed operation of the device was as follows: The cells were first tagged with 10 μm magnetic beads using conventional cell tagging protocols. They were then introduced into the channel to be captured. The magnetic structures would be magnetized in the short axis, making the left and right edges of the structures the "poles" of the magnet. To achieve repeatable release of selected cells, the approach proposed here was to change the location of the north and south poles to locations outside of the channel by changing the magnetization of the structures from the short axis to the long axis. If the poles are sufficiently far from the channel, the attraction force on the cells will become negligible, and they could be released with the flow in the microchannel. To achieve this magnetization switching, we used an external magnet's field for its simplicity and reliability, which was extensively proven in biomedical applications.

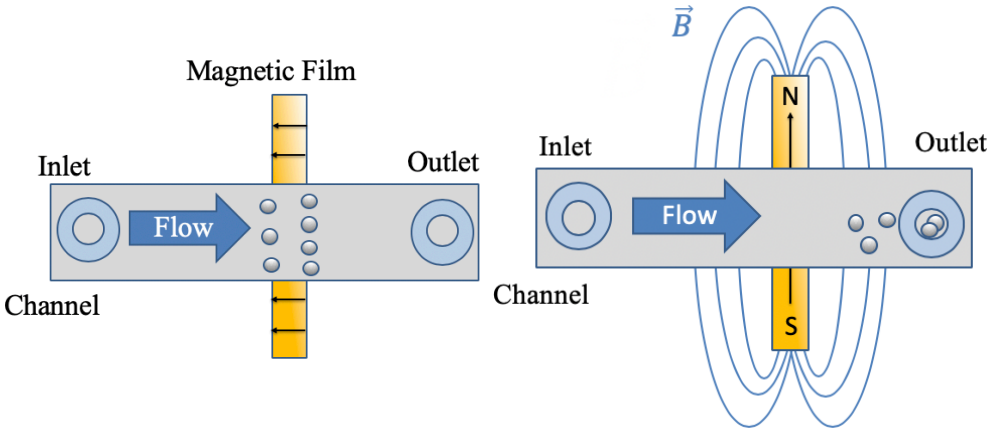

Figure 2-12: Concept of a single magnet for cell manipulation.

2.2.2 A single magnet for individual cell manipulation

After verifying a single magnet's capture and release capability, we shrank down the magnet size to capture a single cell. The magnet was 7 µm x 21 µm x 120 nm, comparable with the 5 µm magnetic bead size. Iron was chosen for the magnet due to its high saturation magnetization and magnetocrystalline anisotropy. Also, the thickness ensured a high enough total magnetic moment to capture a bead. The magnetization was switched between the long and short axis to capture and release beads. To achieve this switching, we used a pulse current and its corresponding Oersted field for its local controlling ability, which was suitable for further array application.

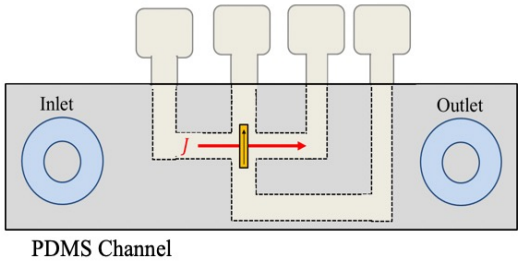

Figure 2-13: Concept of a single magnet for individual cell manipulation.

2.2.3 Array magnets for individual cell manipulation

Finally, after all the steps above, we built a 5×5 array of magnets and designed a controlling circuit. The magnets were identical to the previous design. The magnetization was switched to the short axis to capture, while the magnet was demagnetized to release. This was to avoid capturing beads at the north and south poles of the long axis in release mode. To achieve magnetize or demagnetize the magnet, we used a pulse current but with different magnitudes.

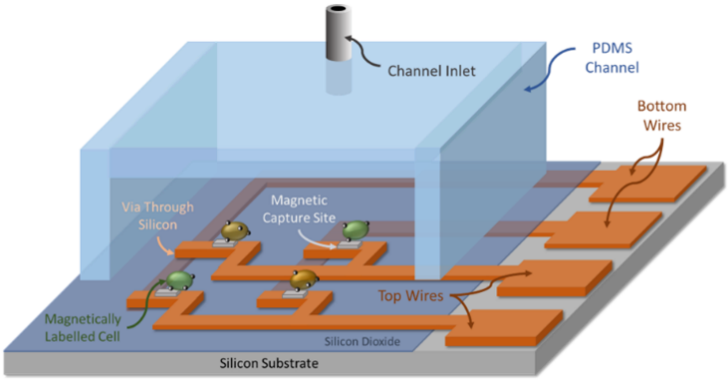

Figure 2-14: Concept of 5×5 array magnets for individual cell manipulation.

2.3 Simulation

2.3.1 Methods

1) Magnetic flux density

To determine the Oersted field from a current-carrying wire, we can use Finite Element methods to calculate it. Here, a simple estimation method is introduced. For an infinite horizontal sheet of charge, if we consider an Ampere loop with a width a to determine the magnetic flux density (positive counter-clockwise), we get:

$$\oint \boldsymbol{B} \cdot d\boldsymbol{s} = Ba \qquad \text{Eq. } 2-1$$

And the dot product is zero for the two sides where the field is perpendicular to the sides. Therefore,

$$2Ba = \mu_0 Ja \qquad \text{Eq. } 2-2$$

$$B = \frac{1}{2}\mu_0 J \qquad \text{Eq. } 2-3$$

Where J is the current sheet density. This is the current-induced magnetic flux density of an infinite sheet of charge. A similar Ampere loop can be used for a finite-width wire. The result is comparable to the FEM solutions. From this, we can determine the magnetization of the magnet.

To determine the magnetic flux density from the magnet, we can use the following dipole equation:

$$\boldsymbol{B} = \frac{\mu_0}{4\pi}\left[\frac{3\boldsymbol{r}(\boldsymbol{m}\cdot\boldsymbol{r})}{r^5} - \frac{\boldsymbol{m}}{r^3}\right] \qquad \text{Eq. } 2-4$$

Where $\boldsymbol{m}$ is the magnetic moment of the magnetic dipole. $\boldsymbol{r}$ is the distance between the magnetic dipole and the point in free space. From the magnetic flux density, we can calculate the magnetic force.

2) Magnetic force

Traditionally, community in biology uses the following form to approximate the magnetic attraction force acting on a magnetic bead from a magnet [87]–[89]:

$$\boldsymbol{F}_{mag} = \frac{V\Delta\chi}{\mu_0}(\boldsymbol{B}\cdot\nabla)\boldsymbol{B} \qquad \text{Eq. } 2-5$$

where V is the volume of the bead, $\Delta\chi$ is the susceptibility difference between the bead and the environment, $\boldsymbol{B}$ is the magnetic flux density generated purely by the magnet, $\boldsymbol{F}_{mag}$ is the magnetic force vector. Magnetic beads usually refer to superparamagnetic iron oxide nanoparticles (SPIONs) [90]. Their susceptibility is around 5 [91], more minor than bulk iron oxide.

It is essential to point out that the equation is based on a dipole model, and it doesn't consider the effect on the magnetic field induced by the bead. [92] If we consider the single-cell sorting case, in which a bead has a similar size as a magnet, the demagnetization field can't be neglected. A more accurate way of obtaining the magnetic force on these beads is to derive the Maxwell stress tensor from the Lorentz Force and Maxwell equations and then integrate it over the bead volume, as shown below. [93][94] Maxwell equations are first given for convenience.

Gauss's law:

$$\nabla \cdot \boldsymbol{E} = \frac{\rho}{\varepsilon_0} \qquad \text{Eq. } 2-6$$

Gauss's law for magnetism:

$$\nabla \cdot \boldsymbol{B} = 0 \qquad \text{Eq. } 2-7$$

Faraday's law:

$$\nabla \times \boldsymbol{E} = -\frac{\partial \boldsymbol{B}}{\partial t} \qquad \text{Eq. } 2-8$$

Ampère's circuital law:

$$\nabla \times \boldsymbol{B} = \mu_0 \boldsymbol{J} + \mu_0 \varepsilon_0 \frac{\partial \boldsymbol{E}}{\partial t} \qquad \text{Eq. } 2-9$$

To derive the Maxwell stress tensor, we start with the Lorentz force law:

$$\boldsymbol{F} = q(\boldsymbol{E} + \boldsymbol{v} \times \boldsymbol{B}) \qquad \text{Eq. } 2-10$$

$$\boldsymbol{F} = \int (\boldsymbol{E} + \boldsymbol{v} \times \boldsymbol{B}) \rho dv \qquad \text{Eq. } 2-11$$

the force per unit volume is:

$$\boldsymbol{f} = \rho \boldsymbol{E} + \boldsymbol{J} \times \boldsymbol{B} \qquad \text{Eq. } 2-12$$

Where ρ is the volume charge density, $\boldsymbol{J}$ is the current density. Notice that $\boldsymbol{J}$ has contributions from both the migration of the carriers relative to the material and the net charge carried by the moving material.

Next, we use Gauss's law and Ampère's circuital law to replace ρ and $\boldsymbol{J}$ with the field terms:

$$\boldsymbol{f} = \varepsilon_0 (\nabla \cdot \boldsymbol{E}) \boldsymbol{E} + \frac{1}{\mu_0} (\nabla \times \boldsymbol{B}) \times \boldsymbol{B} - \varepsilon_0 \frac{\partial \boldsymbol{E}}{\partial t} \times \boldsymbol{B} \qquad \text{Eq. } 2-13$$

If we only consider the static magnetic field, the equation becomes the original Lorentz formalism:

$$\boldsymbol{f} = \frac{1}{\mu_0} (\nabla \times \boldsymbol{B}) \times \boldsymbol{B} \qquad \text{Eq. } 2-14$$

We can then rewrite $\boldsymbol{f}$ more compactly using vector calculus identity and add a symmetry term. For simplicity, we neglect the mathematical derivation and introduce the Maxwell stress tensor:

$$\sigma_{\boldsymbol{ij}} = \frac{1}{\mu_0} B_i B_j - \frac{1}{2\mu_0} \delta_{ij} B^2 \qquad \text{Eq. } 2-15$$

which satisfies

$$\nabla \cdot \boldsymbol{\sigma} = \boldsymbol{f} + \varepsilon_0 \mu_0 \frac{\partial \left(\frac{1}{\mu_0} \boldsymbol{E} \times \boldsymbol{B}\right)}{\partial t} \qquad \text{Eq. } 2-16$$

For equation 2-15, the first term is the magnetic tension, and the second is the magnetic pressure force. For equation 2-16, the second term is the time derivative of the EM field's momentum density. The first term is the time derivative of the massive particles' momentum density. So, the physical meaning of this equation is the law of conservation of momentum.

The Maxwell stress must be integrated over the volume and the solid/vacuum interface to calculate the total force F on the bead. In the stationary case, according to the equilibrium equation, the force balance, and Gauss' theorem, we get:

$$\nabla \cdot \boldsymbol{\sigma_1} + \boldsymbol{f}_{body} = \rho \boldsymbol{a} \qquad \text{Eq. } 2-17$$

$$\boldsymbol{n_1}(\boldsymbol{\sigma_2} - \boldsymbol{\sigma_1}) = 0 \qquad \text{Eq. } 2-18$$

$$\int \left(\nabla \cdot \boldsymbol{\sigma_1} + \boldsymbol{f}_{body}\right) dV + \oint \boldsymbol{n_1}(\boldsymbol{\sigma_2} - \boldsymbol{\sigma_1}) dS = 0 \qquad \text{Eq. } 2-19$$

Here 1 means inside the solid, and 2 means in the vacuum. Then the total force is given by:

$$F_{mag} = -\int \boldsymbol{f}_{body} dV = \oint \boldsymbol{n_1 \sigma_2} dS \qquad \text{Eq. } 2-20$$

To summarize, the total magnetic force can be computed from the outside boundary as a surface integral of the Maxwell stress tensor. In a vacuum, we don't need to consider relative permittivity.

Now, we can look back at equation 2-5. It seems to be equation with the following assumption:

$$\boldsymbol{M} = \Delta\chi\boldsymbol{H}, \boldsymbol{F} = V\boldsymbol{f} \qquad \text{Eq. } 2-21$$

Meaning that the captured bead does not change the original distribution of the magnet's B-field, and the force distribution is uniform inside the bead. However, under the circumstance of single-cell manipulation, in which the bead size is comparable to the magnet size, these assumptions are unreliable. The FEM results given later will show discrepancy between different approaches.

3) Fluidic force

The Reynolds number describes the ratio of inertial force with respect to viscous forces:

$$Re = \frac{\rho v D}{\eta} \qquad \text{Eq. } 2-22$$

For a magnetic bead in the fluid, ρ is the fluid density, v is the cell velocity relative to the fluid, D is the bead's characteristic length, η is the fluid viscosity. The result is a Reynolds number of roughly 0.2-1 so that the drag force equation in Stokes flow can be applied. In our case, it is 4.

$$F_{drag} = 6\pi\eta R v \qquad \text{Eq. } 2-23$$

where R is the bead's radius, η is the fluid viscosity, v is the cell velocity relative to the fluid. By comparing F_{mag} with F_{drag}, we can determine whether beads will be captured [94]. By setting drag force and gravity force equal, $F_{drag} = F_g$, we can find the natural sedimentation speed of the beads within the fluid to be about 3 μm/s. Sometimes we flip the device for better observation.

This indicates if that for a channel with a height of 300 μm, we need to wait for 2 minutes until all beads get to the bottom before initiating cell sorting. That is important because the magnetic field is quite localized, and the magnet can only attract beads that are within around 20 μm range.

The length of time for beads to react to the fluid can also be characterized, during which inertial effects play a role. It is calculated based on momentum:

$$t = \frac{mv}{F_{drag}} = \frac{mv}{6\pi\eta Rv} = \frac{2\rho_{bead}R^2}{9\eta} \qquad \text{Eq. } 2-24$$

The result is about 5 μs, from which we conclude that the relaxation time is negligibly short and can be omitted in motion analysis. We can also recall that the magnetization switching time is around the nanosecond scale, which is shorter than the mechanical response time. Therefore, the relaxation time is also omitted in dynamic magnetization analysis. This means that the bead motion can be considered a quasi-static process.

2.3.2 Stationary magnetic model

The structures were simulated using two different methods: the dipole method in MATLAB and the finite element method in COMSOL. Figure 2-13 shows the simulation setup. In Figure 2-15a, the circle represents a magnet with a magnetic dipole moment pointing upward. In this simulation, the beads are assumed to be infinitesimally small. In Figure 2-15b, the magnet and the beads have a finite volume, and the force is calculated by integration. Figures 2-15c and 2-15d show that the magnetic flux density calculated using equations correlates well with the simulation results. However, as discussed previously, the dipole assumption leads to significant errors in the

calculation of the magnetic force. Therefore, the COMSOL model was used as the benchmark to conduct the static and dynamic force studies.

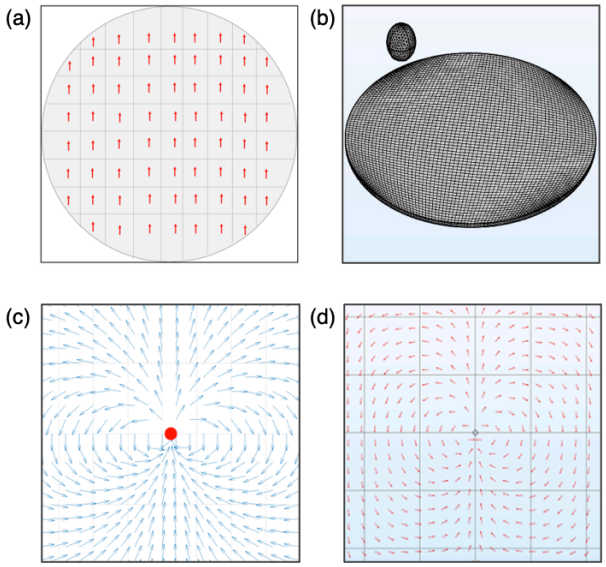

Figure 2-15: (a) MATLAB simulation setup. (b) COMSOL simulation setup. (c) Magnetic flux density from MATLAB. (d) Magnetic Flux density from COMSOL.

To determine the magnet's ability to capture objects, we modeled the static magnetic force between an iron magnet measuring 7 µm by 21 µm and a superparamagnetic bead of 8.5 µm diameter using boundary element methods (BEM) in COMSOL. This method only requires a surface mesh, so a volumetric air mesh was not necessary. It was more computationally efficient while maintaining the same level of accuracy. The bead was composed of a non-magnetic polymer core and a magnetic shell, and its nonlinear B-H curve was manually coded from the datasheet. The remnant magnetization of 800 emu/cc was also included in the model. The resulting capture force was approximately 30 pN at the left and right sides of the magnet. In the release state, the force was

close to zero. The difference between these two configurations indicates the two different states of the system. A parametric study was also conducted to investigate the effect of the bead position and magnet thickness on the 3D magnetic force distribution. This study led to the current design of the magnet thickness and showed that it can generate a sufficient magnetic field gradient to immobilize magnetic beads within a certain height range.

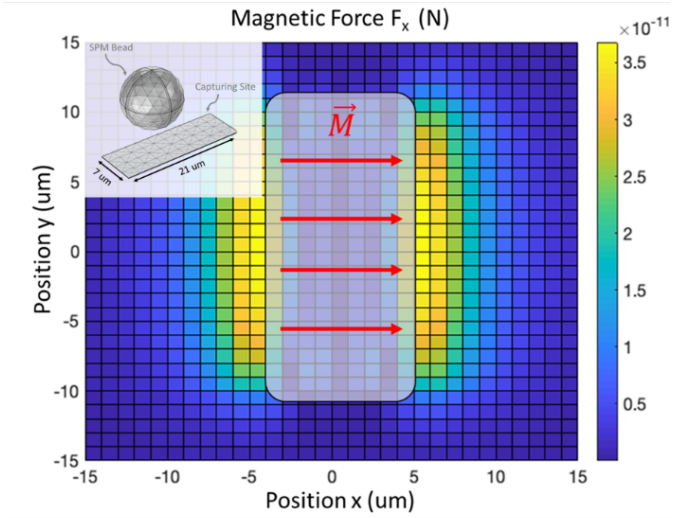

Figure 2-16: Capture state magnetic force spatial distribution.

2.3.3 Dynamic magnetic model

To further analyze the design, a dynamic model of a magnet and an SPM bead was created using finite element method (FEM). The surrounding liquid and air environment and perfectly matched layers were included in the model. The magnet was fixed on the substrate and could be set to have either zero or remanent magnetization in different states. The SPM bead, which had the same properties as the static model, was positioned in the microfluidic channel. Newton's laws were

used to describe the movement of the bead, and the mesh was set as deformable. A separate flow distribution model was used to obtain the flow rate at different heights and to incorporate the Stokes drag force into the model. At each time step, global ordinary differential equations were solved to calculate the magnetic force. The net force and acceleration were then determined by adding the corresponding drag force. This provided the x-y coordinates of the bead in the next time step. By iterating this process, the time-dependent trajectory of the bead was obtained. Figure 2-17 shows the side view of the channel and the simulation setup for the dynamic model.

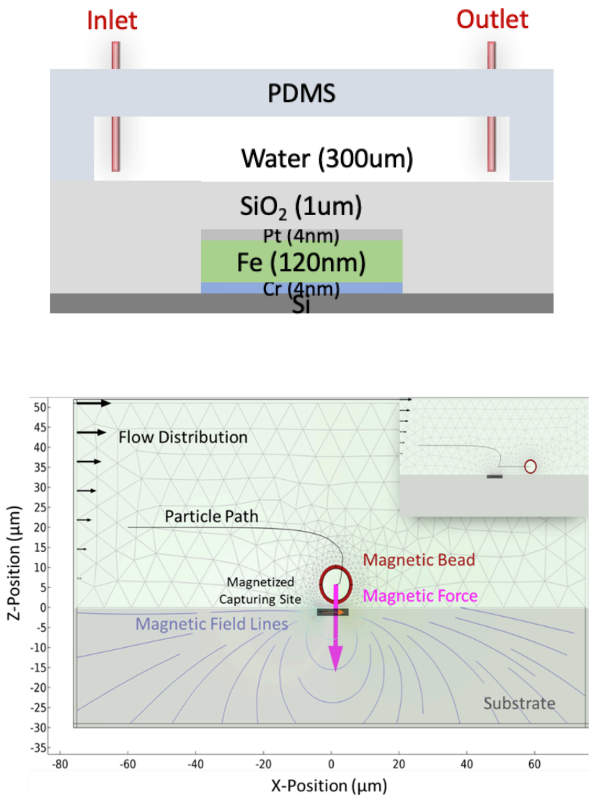

Figure 2-17: Device from the side view and the dynamic model's simulation setup.

The dynamic model allowed us to visualize the capture-release process and greatly increased our ability to optimize the design. For example, we can magnetize the magnet as the beads approach. We can also observe the exponentially increasing magnetic force as the bead moves from 20 µm to 0 µm (captured state). The model also enables us to determine the critical flow rate (20 µL/min) and the critical release height of beads (20 µm), which is just high enough to avoid capture, as shown in Figures 2-18 and 2-19. This information is valuable for optimizing the design and achieving the desired capture and release behavior.

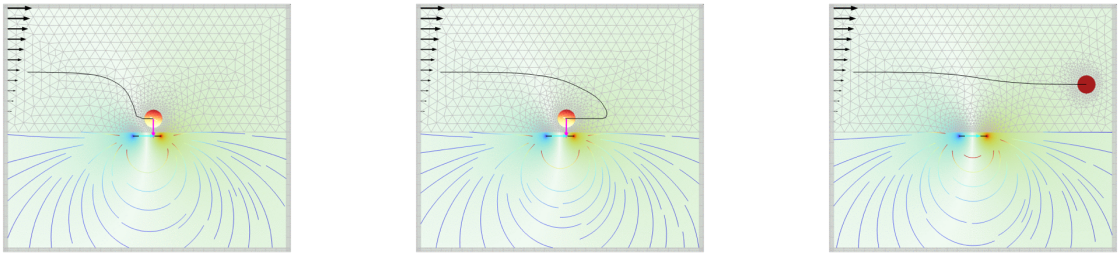

Figure 2-18: Bead trajectory under flow rates of 3µL/min, 15µL/min, 20µL/min.

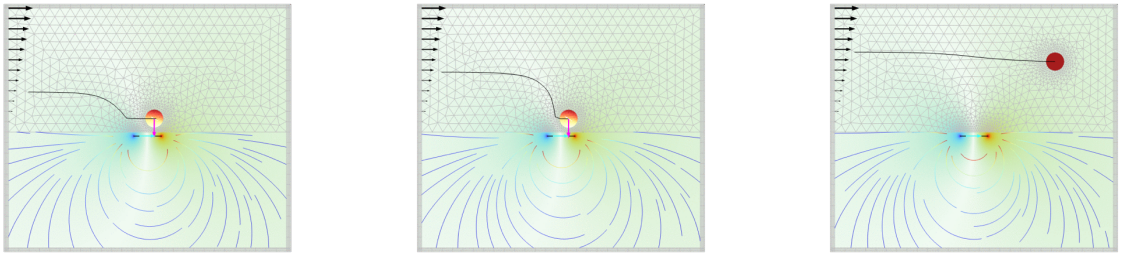

Figure 2-19: Bead trajectory with release heights of 10µm, 15µm, 20µm.

Combining all of the above data, we created a bead capture color map. Figure 2-20 shows the map, where the x-axis represents the flow rate and the y-axis represents the initial bead release height. Each block in the map corresponds to a different study case. White blocks indicate that the bead will be captured under the corresponding conditions, while black blocks indicate that the bead will not be captured. This plot takes into account the coupling effect between flow rate and height, which cannot be assessed using a stationary model. Other factors, such as the magnet's height, can also be included in the analysis.

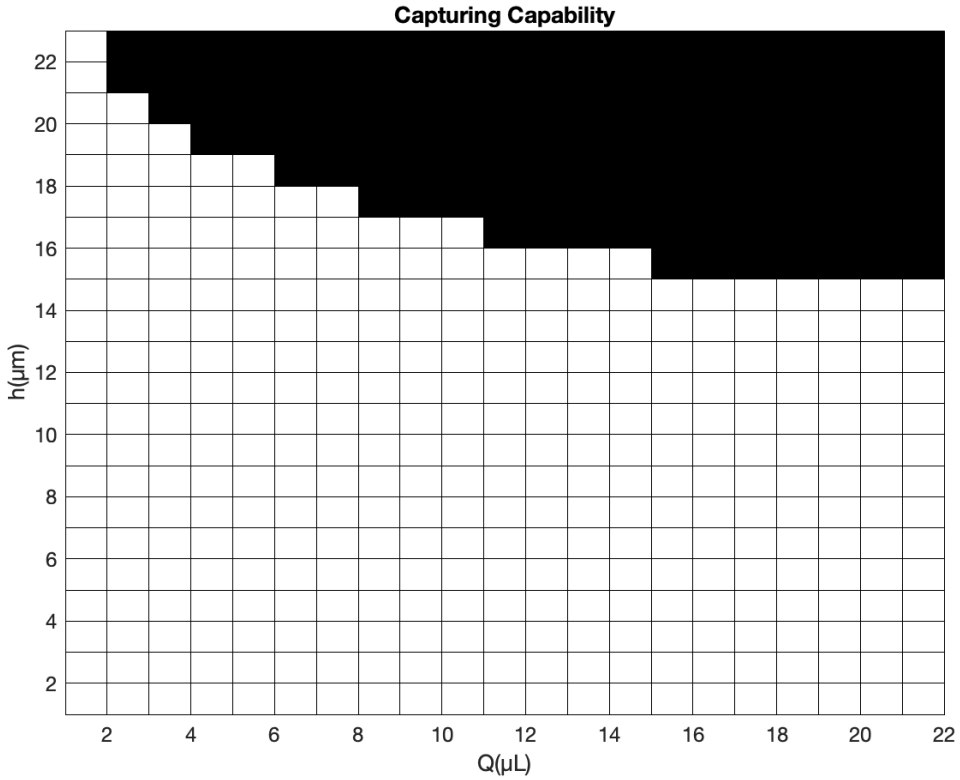

Figure 2-20: Bead capture color map, with white block indicating captured while black ones indicating not captured.

2.3.4 Supporting models

1) Oersted field model

To determine the electric currents needed to generate the magnetizing and demagnetizing fields, we modeled the spatial distribution of the Oersted field generated by a current-carrying copper wire using FEM. The model consisted of a 25-μm wide and 1-μm thick copper wire surrounded by air. Perfectly matched layers were applied at the exterior boundary to mimic an infinite environment. The terminal condition was applied at one end of the wire, while the other end was grounded. The current flowed through the wire uniformly. A probe located at the top surface of the wire (i.e., the magnet's position) was used to measure the magnetic field strength and determine the currents needed to generate the 500 Oe and -120 Oe magnetizing and demagnetizing fields. The simulation results indicated that 2 A and -1 A currents generated 480 Oe and -120 Oe, respectively. The magnetic field strength increases linearly inside the wire, reaches a maximum at the interface between the wire and the air, and decays in the air following the inverse square law. Inside the magnet, the field strength is almost constant. There is a sudden change in the field strength at the interface between the magnet and the air due to the high relative permeability of the magnet. Finally, a controlled study was conducted to ensure that the captured magnetic bead only slightly affects the current-induced magnetic field distribution, as shown in Figure 2-21.

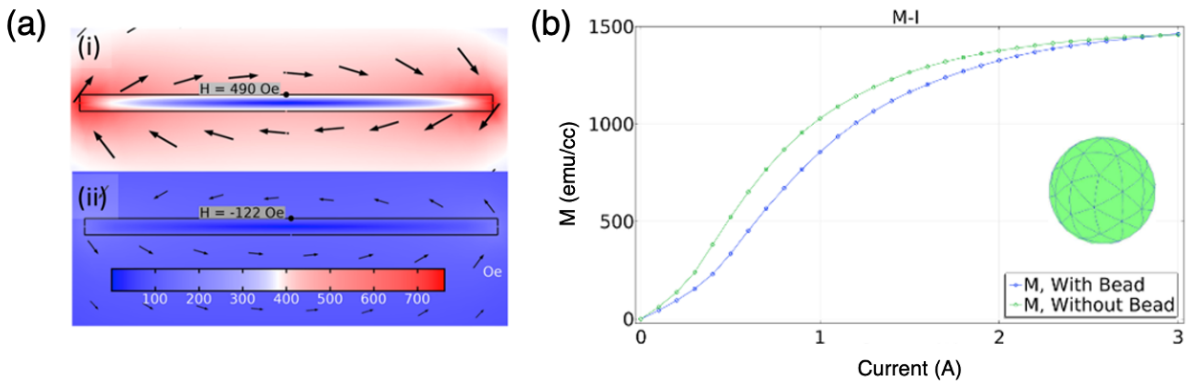

Figure 2-21: (a) Steady-current induced Oersted field. The number indicates the required field to magnetize or demagnetize the Fe magnet. (b) The relationship between magnetization and the current with a control group including a captured magnetic bead.

2) Fluidic model

A separate flow distribution model was used to obtain the flow rate at different heights and the corresponding Stokes drag force. The polynomial approximation was integrated into the dynamic magnetic model to simplify the solution of the Navier-Stokes equations.

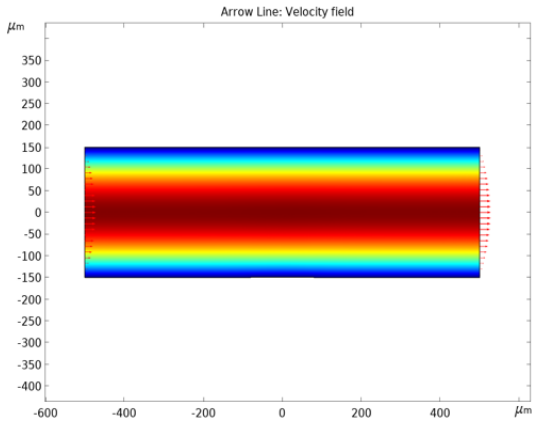

Figure 2-22: Flow rate distribution in the channel (side view).

3) Electrical heat model

A separate heat model was also conducted to ensure that the circuit would not generate excessive heat that could melt the magnet or boil the water. It was determined that a pulse current with a duration of less than 0.2 seconds was safe for the device and was also long enough to switch the magnetization, as the precession occurs within the nanosecond range.

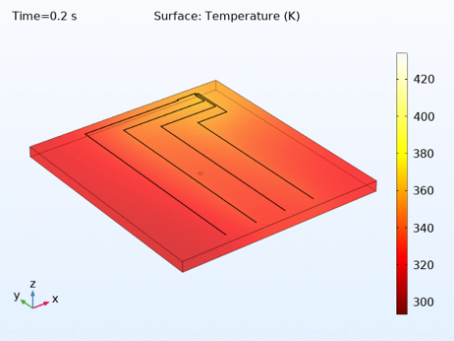

Figure 2-23: Electrical heat generation in the circuit and heat dissipation inside the device.

2.4 Fabrication

The fabrication procedure and images of the fabricated devices are shown in Figure 1. The device was built on a 3 x 4 cm^2 bare silicon substrate. The substrate was cleaned with acetone, methanol, and isopropanol to remove any organic contaminants from the surface before the subsequent microfabrication steps. The bottom electrode layer was first patterned using a standard negative resist (AZ nLOF2020) and a contact photolithography process (Karl Suss MA-6 Contact Aligner). The [Ti(5nm)/Cu(600nm)/Ti(10nm)] bottom electrode stack was deposited using e-beam evaporation (CHA Solutions) and patterned using liftoff with NMP as the resist stripper. Above

this first electrode layer, we deposited a layer of PECVD silicon nitride and silicon dioxide (80nm/200nm) (STS PECVD). We then wet-etched vias through this oxide layer using a buffered oxide etch (BOE). The etch was masked using a negative photoresist etching mask that was patterned using the same photolithography process described above. The top electrode stack [Ti(5nm)/Cu(1µm)/Ti(10nm)] was deposited and patterned using the same liftoff procedure described for the bottom electrodes. The magnetic capturing site stack [Ti(5 nm)/Fe(120 nm)/Ti(10 nm)] was again patterned with the same photolithography and liftoff procedure. To passivate the surface of the device and prevent interactions between these layers and the fluid in the microchannel, we deposited another thicker layer of PECVD silicon dioxide (1µm) on top of everything. Finally, the contact electrodes were exposed by etching this passivating silicon dioxide layer using BOE with a negative photoresist etching mask. The fabrication steps and the final 5×5 array device is shown in Figure 2-24.

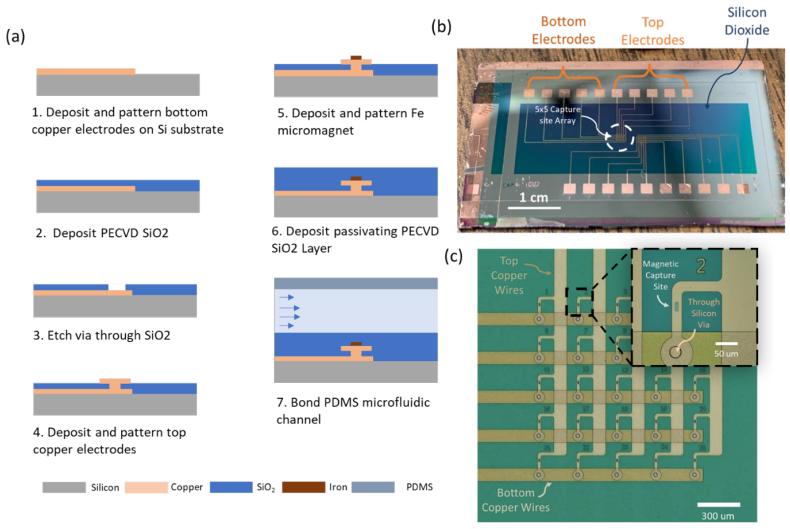

Figure 2-24: Fabrication steps and the final device.

The development process consisted of several stages, as shown in Figure 2-25. In the final device, each magnet can be individually controlled. Green magnets capture beads, red magnets release beads, and blue magnets are in the process of releasing beads.

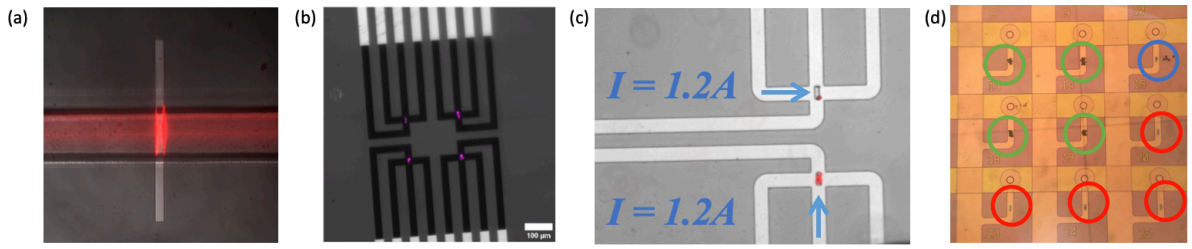

Figure 2-25: (a) A single magnet for cell manipulation, under the fluorescent view. (b)A single magnet for individual cell manipulation, under the fluorescent view. (c) A single magnet for individual cell manipulation. (d) Array magnets for individual cell manipulation.

We also encountered several challenges during the fabrication and testing process, including fading, peeling, oxidation, and electrochemical reactions.

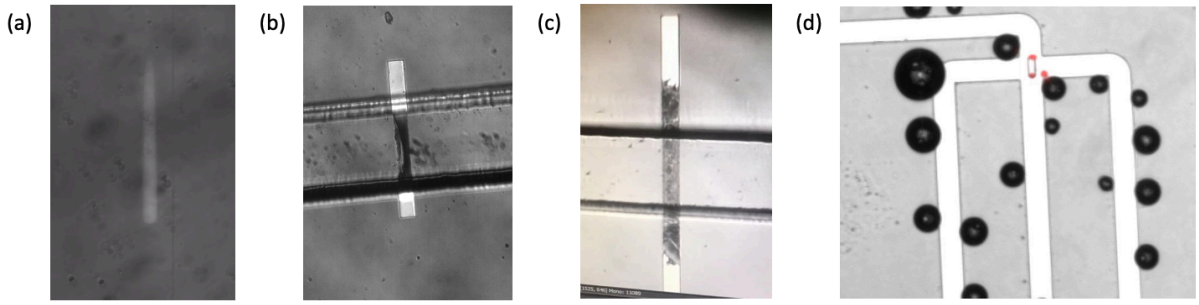

Figure 2-26: (a) Fading (b) Peeling off (c) Oxidation (d) Electrochemical reaction.

2.5 Results and discussion

1) Magnetic characterization

To obtain the coercivity and saturation fields of the patterned Fe magnet, we performed a SQUID test. The results were used in the models to inform the design of the device and determine the values of various variables during testing. The magnetic force microscopy (MFM) images showed that the magnet could be successfully magnetized and demagnetized using the prescribed current pulse.

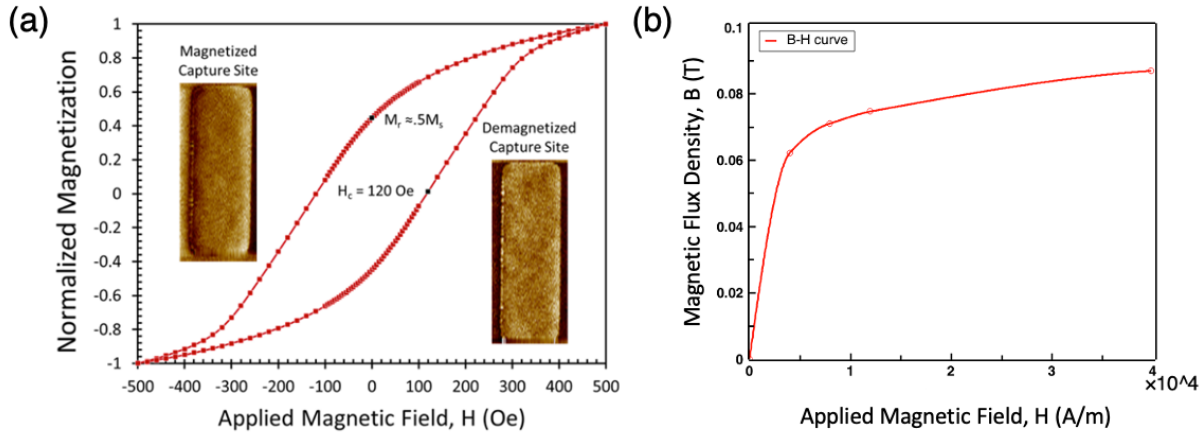

Figure 2-27: (a) SQUID and MFM data of the patterned Fe magnet. (b) B-H curve of beads.

2) Beads capture and release

After verifying the magnetization and demagnetization of individual capture sites, we performed experiments to evaluate the ability of our device to capture and release cells. Since working with live cells is more complex, we first tested the platform using only superparamagnetic beads. To better mimic the behavior of cells, we used 8.5-µm SPM beads as a substitute because they have a similar diameter to that of a cell and therefore exert a similar drag force in the fluid.

In this experiment, we first initialized all of the capture sites to the magnetic capture state by running 2-amp currents underneath each capture site. We then introduced the magnetic bead solution into the channel using a syringe pump with a flow rate of 30 μL/min. As the beads flowed through the channel, they settled to the bottom due to their higher density compared to the suspension solution. Once at the bottom, the beads flowed near the capturing sites until the magnetic attraction between the bead and a nearby site was strong enough to capture and hold it. This process continued until all of the capturing sites had captured the maximum number of beads they could hold.

Next, we released the beads captured at each site, starting from capture site 25, by running a 1-amp current opposite to the magnetizing current. The results of this experiment are shown in Figure 2-26, where we see the sequential release of beads from 8 different capture sites. This experiment demonstrated that the magnetic attraction between an 8.5-μm magnetic bead and a magnetized capture site was sufficient to immobilize it at a flow rate of 30 μL/min. Additionally, it showed that we could deterministically release the captured beads on any desired capture site by using a -1-amp current pulse.

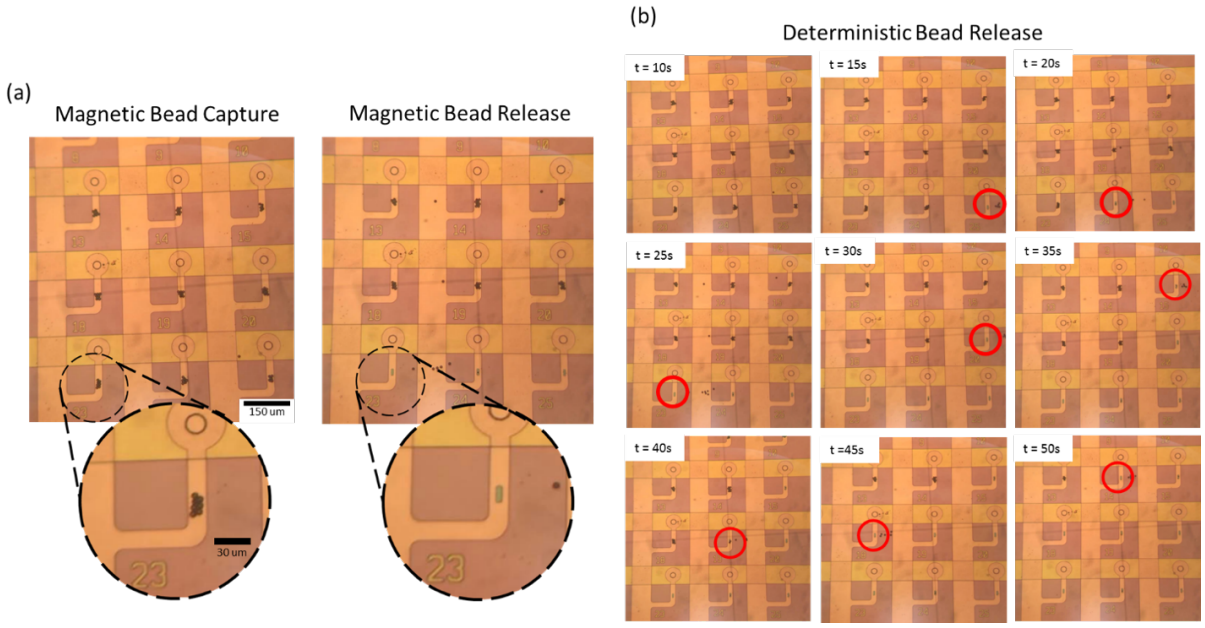

Figure 2-28: Magnetic beads capture and release illustration.

3) Cells capture and release

To further validate the operation of this platform, we demonstrated its ability to capture and release magnetically functionalized cells. Using standard immunomagnetic labeling procedures, we labeled Jurkat T-cells with 8.5-µm SPM beads. Since these labeling procedures are imperfect, the cell solution consisted of labeled cells, unlabeled cells, and free SPM beads. Approximately only 30% of cells in the solution were successfully labeled with SPM beads.

Before introducing the cells into the channel, the capture sites were magnetized using 2-amp current pulses. The cell solution was introduced into the device at a flow rate of 30 µL/min. Due to the low concentration of labeled cells and free SPM beads, we had to wait about 5 minutes to observe successful cell capture at most of the capture sites (Figure 2-29).

After verifying successful cell capture, we began the release process. We demagnetized each capture site with cells one at a time using the same -1-amp current pulse described previously. As soon as this current was applied, the captured cells were successfully released as the drag force overcame the magnetic capturing force. This process was repeated for all of the captured cells. The result video of this experiment can be found in the journal paper.

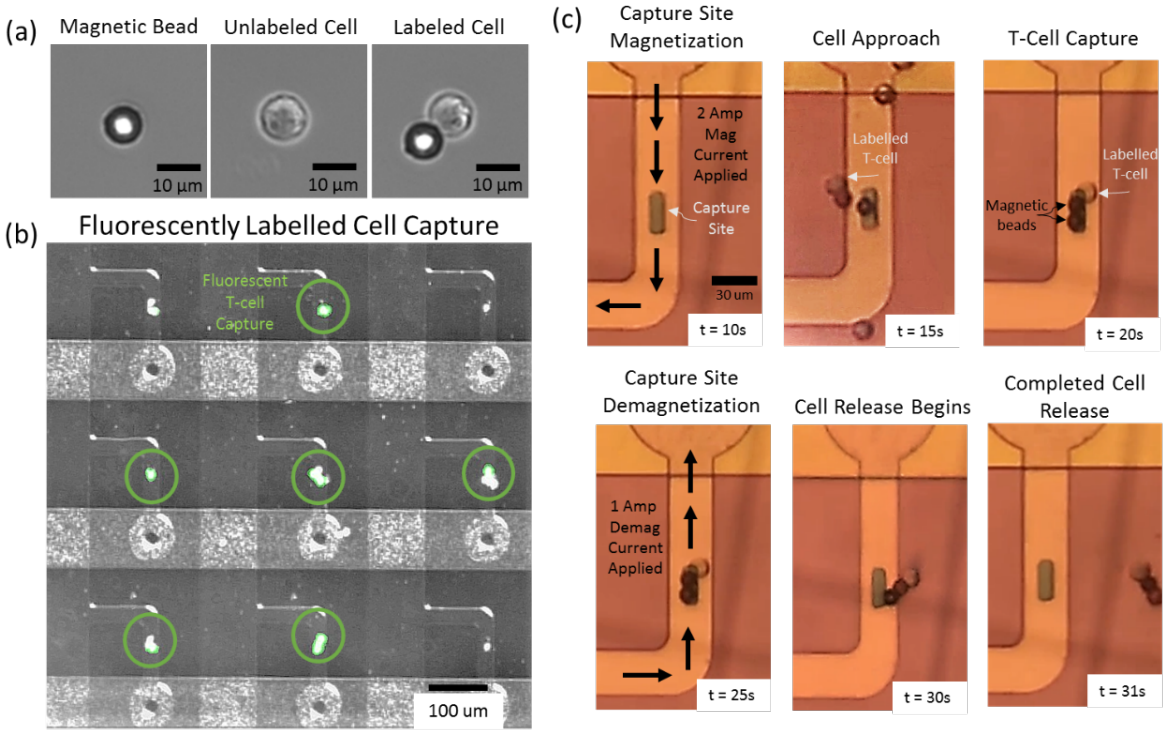

Figure 2-29: Cells capture and release illustration.

Chapter 3. Acoustic Resonators

3.1 Introduction

In recent years, the development of medical implantable devices has focused on compact antennas that operate at the allocated frequency of 400 MHz for real-time through tissue communication. Conventional antennas rely on electromagnetic resonance, which limits their size to the free space wavelength. Electrically small antennas (ESAs) that are smaller than λ/10 at ultra-high frequencies have been proposed as a solution for reducing size, [95]–[97] but these devices still face challenges, such as sensitivity to ground plane effects and reduced radiation efficiency, particularly in electrically lossy environments like the human body. To address these challenges, magnetoelectric (ME) antennas have been proposed. [98]–[103] These antennas rely on acoustic resonance, [104], [105] allowing for better miniaturization. Several studies have demonstrated their ability to create significant magnetization changes in small form factors. The radiation from a magnetic dipole also decays less than that from an electric dipole in the human body. [106]–[115]

Thin film devices based on mechanical resonance, such as bulk acoustic wave (BAW) resonators [116]–[118], have been widely used due to their high-quality factor. However, their high operating frequency makes them unsuitable for the medical implant communication service (MICS) band. Recently, a new design called a laterally excited bulk-wave resonator (XBAR) [119]–[122] has been developed that is more compatible with complementary metal-oxide-semiconductor (CMOS) technology and has strong piezoelectric coupling. In addition, it has demonstrated unique features

in the A0 mode in the 400 MHz region, such as high velocity, low dispersion, and robustness over temperature changes.

In this work, a 400 MHz XBAR ME antenna design based on an acoustic lamb wave was proposed. The resonator utilized a magnetostrictive and piezoelectric heterostructure membrane. Experimental results demonstrated the antenna's high electromechanical coupling. Finite element method (FEM) simulation was carried out for both transmission and reception modes to maximize resonance in the A0 mode. A micromagnetic model and a dipole model were used to estimate the magnetization change and the radiation strength. These results indicated that the design operated under mechanical resonance and generated detectable magnetic signals, providing a new solution for miniaturizing implantable device antennas.

3.2 Proposed design

The XBAR ME antenna is a released sandwich structure consisting of a Pt bottom electrode, an AlN piezoelectric layer, and Al quarter wavelength wide top electrodes, as shown in Figure 3-1. The FeGaB magnetic strips operate as the radiation source. Strips are placed between each top Al metal strip to ensure in-phase tensile or compressive strain. The width of both the Al and FeGaB strips is 5.4 μm, which is a quarter wavelength at 400 MHz. The strips are 1000 μm long. Etching vias are placed in the middle to release the AlN layer and enhance resonance strain.

Unlike common thin-film bulk acoustic wave resonators (FBARs) [123] which work in the thickness-excited S1 mode in the GHz range, the lamb wave antenna operates in the in-plane A0 mode. This design reduces the frequency dependence on the membrane thickness and provides

more compatibility with CMOS technology. The FeGaB strips and AlN film exhibit lateral excitation of strain and electric field, respectively. The use of a micromagnet arrangement ensures a uniform strain for coherent magnetization switching.

The addition of a bottom electrode allows for the transformation into a longitudinal wave (LW) with an out-of-plane E-field, providing stronger electromechanical coupling compared to classical interdigital transducers (IDT) with an in-plane E-field and no bottom electrode. This configuration also has less technological complexity compared to the IDT over-floating configuration with top electrodes for both positive and negative voltage ports and a bottom electrode.

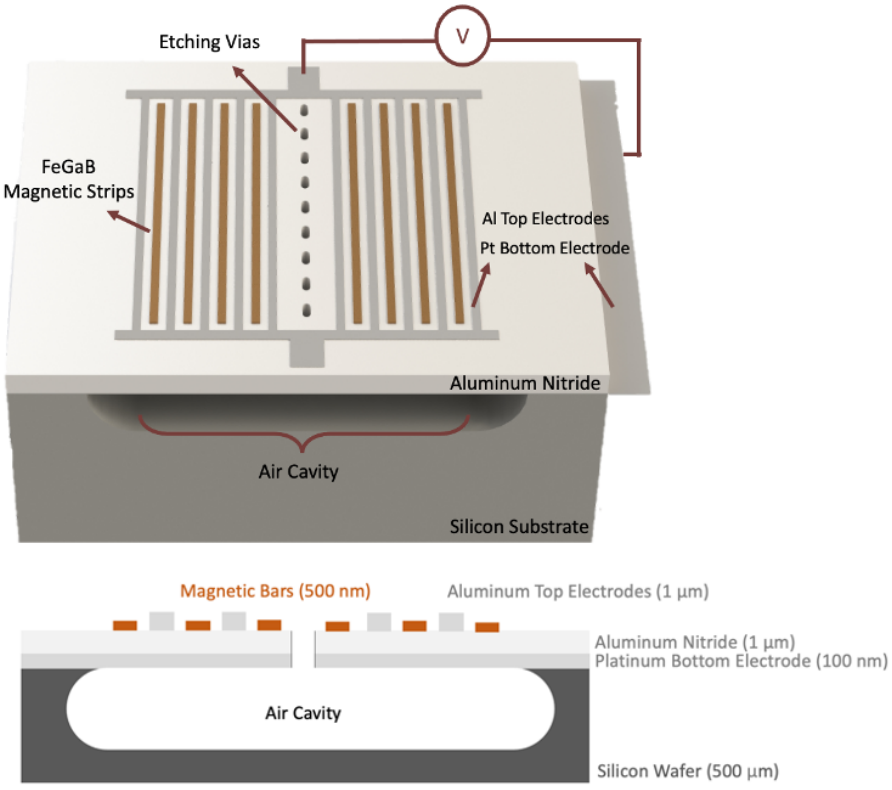

Figure 3-1: 400 MHz XBAR ME antenna design.

3.3 Simulation

3.3.1 Methods

1) Lamb wave

Lamb waves are elastic waves that propagate in solid plates or spheres. The particle motion of these waves lies in the plane that contains the direction of wave propagation and the direction perpendicular to the plate. To model guided wave propagation in physical acoustics, we seek sinusoidal solutions to the wave equation for linear elastic waves that satisfy the boundary conditions. Lamb's equations were derived by considering a solid plate that has infinite extent in the x and y directions, but a finite thickness d in the z-direction. Sinusoidal solutions to the wave equation were assumed, with x- and z-displacements of the form [124]:

$$\xi = A_x f_x(z) e^{i(\omega t - kx)} \qquad \text{Eq. } 3-1$$

$$\zeta = A_z f_z(z) e^{i(\omega t - kx)} \qquad \text{Eq. } 3-2$$

The equation describes sinusoidal waves that have a wavelength k of 2π/k and a frequency of ω/2π. The displacement of these waves is a function of x, z, and t only, and there is no displacement in the y direction or any variation of physical quantities in that direction.

2) Piezoelectrics

$$\boldsymbol{\varepsilon} = s_E \boldsymbol{\sigma} + d^t \boldsymbol{E} \qquad \text{Eq. } 3-3$$

$$\boldsymbol{D} = d\boldsymbol{\sigma} + \varepsilon_\sigma \boldsymbol{E} \qquad \text{Eq. } 3-4$$

where d is the matrix for the direct piezoelectric effect and the superscript t stands for transposition of a matrix. s_E is the compliance matrix under a constant electric field; ε_σ is the permittivity under a constant stress field.

3) Electromagnetics

EM fields are solved in the frequency domain. The governing equation is derived from Maxwell's equations. The equation solves for the resonance of a structure under the assumption that there is negligible radiation. As a result, the radiation from the piezoelectric layer and the transmission line are not considered in the piezoelectric strain analysis.

$$\nabla \times (\mu^{-1} \nabla \times \boldsymbol{A}) = -(j\omega\sigma - \omega^2 \varepsilon)\boldsymbol{A} \qquad \text{Eq. } 3-5$$

Where $\boldsymbol{A}$ is the vector potential. σ is the conductivity. ε is the permittivity.

4) Magnetics

The radial component of the magnetic field generated by a magnetic dipole is given as follows:

$$H_r = j\frac{ka^2 I_0 cos\theta}{2r^2}\left(1 + \frac{1}{jkr}\right)e^{-jkr} \qquad \text{Eq. } 3-6$$

Where I_0 is the equivalent current of the magnetic dipole.

The magnetostriction from the applied field is given as follows:

$$\varepsilon_{me} = \frac{3}{2}\frac{\lambda_s}{M_s^2} dev(\boldsymbol{M} \otimes \boldsymbol{M}) \qquad \text{Eq. } 3-7$$

Where λ_s is the saturation magnetostriction and M_s is the saturation magnetization. The symbol is the derivative of magnetization tensor product.

3.3.2 Transmission mode

To predict the resonance response of the XBAR ME antenna in transmission mode, a finite element analysis (FEA) was performed. Electrostatic and solid mechanics modules were used in the analysis. Piezoelectricity and transmission loss were also taken into account. The resonator and the bus line were modeled in 3D form, surrounded by perfectly matched layers, as shown in Figure 3-2. The etching vias and the cavity were explicitly modeled as well. The terminal boundary condition with a constant power of 1 mW as input was applied at one side of the Al transmission line, representing the GSG probe. The A0 lamb wave shape could be seen in the graph, which exhibited no critical cut-off frequency at zero wavenumber and has low velocity dispersion. This suggested that the proposed design has a high electromechanical coupling factor and operates in the desired frequency range.

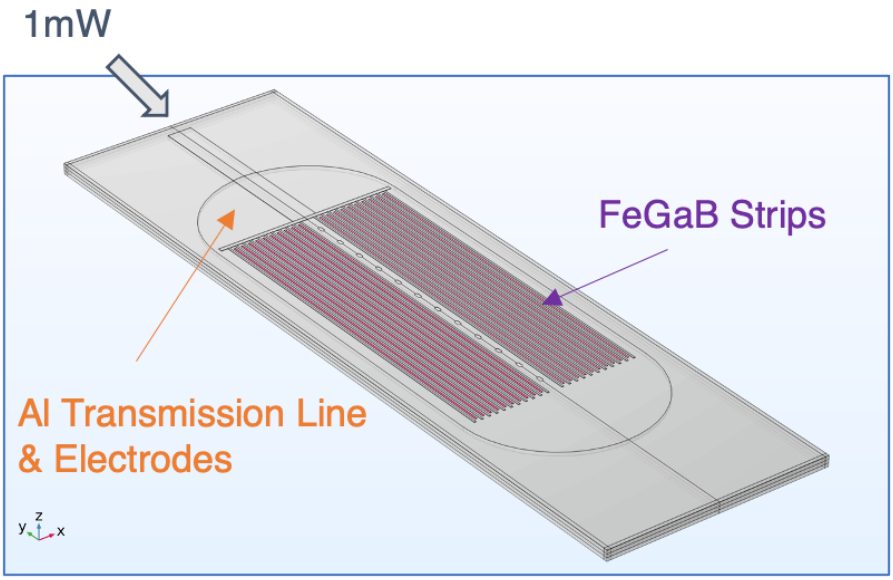

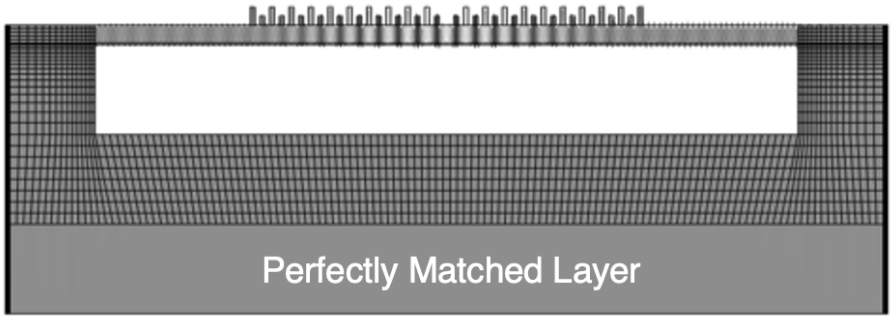

Figure 3-2: Simulation setup and mesh settings.

1) Strain

In the transmission mode, the device functioned by applying a perpendicular electrical field along the c-axis of the crystalline AlN, generating a standing lamb wave. This wave was mechanically coupled with magnetic FeGaB microelements, causing a reorientation of the magnetization and the propagation of the magnetic field. In the reception mode, the principle was the same but in reverse. It should be noted that the nonlinearity of magnetization reorientation causes these two modes to not be perfectly reciprocal.

The impedance, with both real and imaginary components, was plotted in Figure 3-3 and fitted to the experimentally obtained data. The fitted parameters were the mechanical damping and the dielectric loss. The average strain of the FeGaB strips was then calculated. As shown in Figure 3-3, the average strain in the x direction dominates, which is the lateral direction. The device achieved a high quality factor of 500, compared to the typical value of 100 for common SAW structures [125]. This strain was used as the input for the next micromagnetic model.

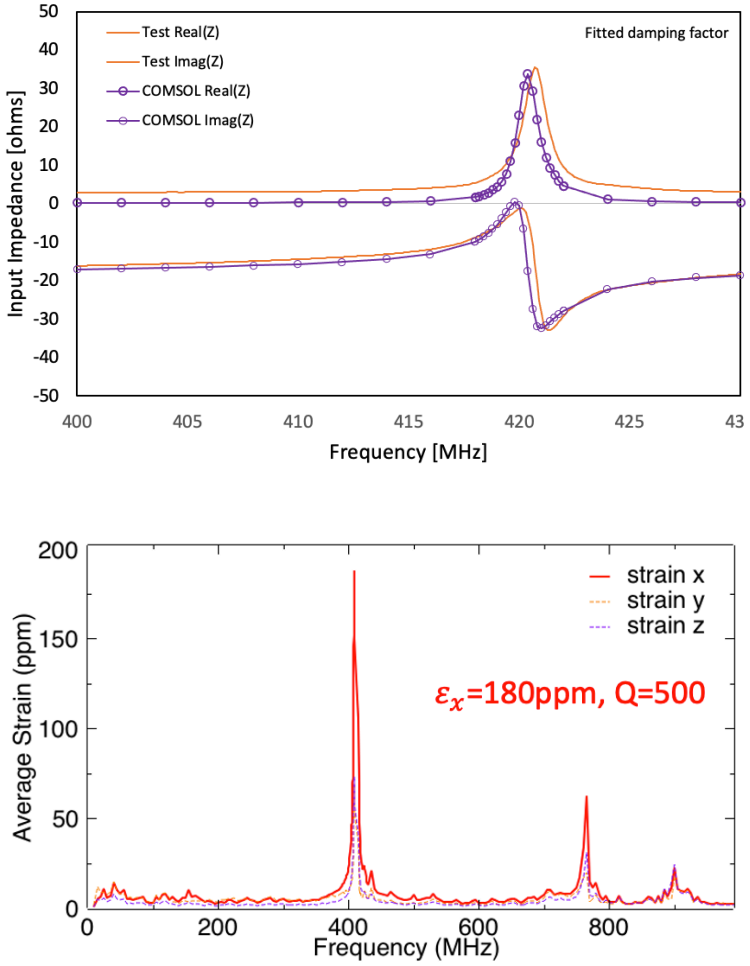

Figure 3-3: Impedance calculation and the average strain of FeGaB strips.

Optimization was performed to maximize the strain experienced by the magnetoelastic elements in the MICS band. The optimized design parameters included the width and thickness of the electrodes, the width and thickness of the magnetic material, and the distance between elements. For example, increasing the number of FeGaB strips resulted in a decrease in the resonant frequency and some periodic variation in the average strain, as shown in Figure 3-4. Other factors, such as the length of the strips, were also considered. The final design was a compromise between

geometric and fabrication considerations, taking into account all relevant boundary conditions, such as air cavities and reflectors.

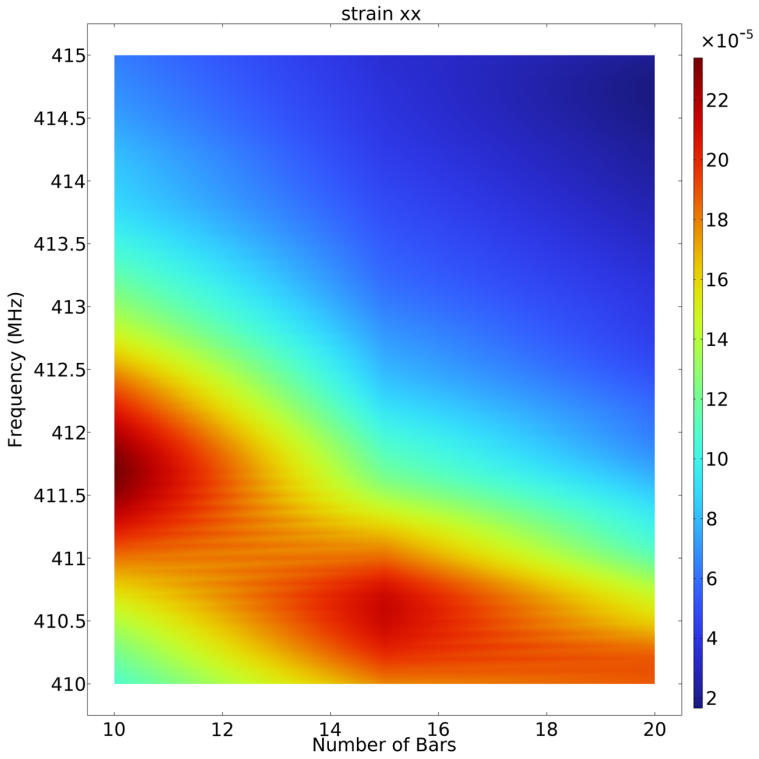

Figure 3-4: Resonant frequency and average strain variation with different numbers of FeGaB strips.

2) Magnetization

The maximum dynamic strain was input into a micromagnetic model to calculate the magnetization change. The Landau-Lifshitz-Gilbert (LLG) equation was used, with the effective field including the magnetoelastic field, the demagnetization field, the Zeeman field, and the exchange field. Only a portion of one magnetic strip was modeled with periodic boundary conditions on the top and bottom. Thus, it is an accurate representation of the strip. The

magnetization was initially released in an arbitrary direction, but quickly oriented along the long axis (y-axis) due to shape anisotropy. A strong bias magnetic field at 45° was then applied to ensure maximum coupling. 45° was proved to be the maximum coupling angle. After all domains were aligned, the bias field magnitude was reduced to avoid pinning effects. The dynamic strain was then applied in the x-axis, causing the magnetization to oscillate. The results, shown in Figure 3-5, demonstrated coherent magnetization switching with a 10% variation in each cycle.

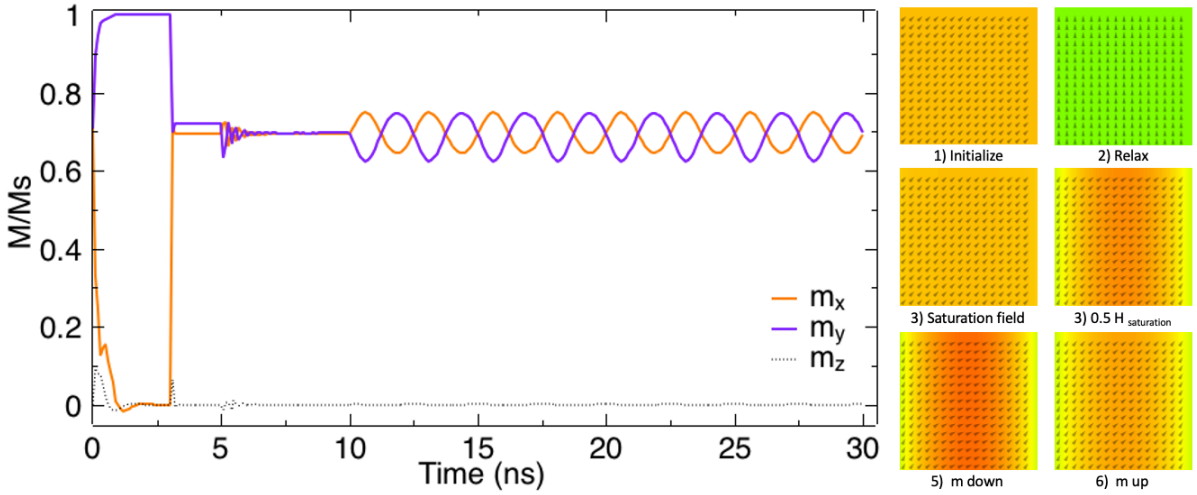

Figure 3-5: Magnetization precession under dynamic strain and a 45° bias field.

3) Radiation

To determine if the amount of magnetic material could produce a detectable signal above the ambient noise threshold, the magnetization change from the micromagnetic model was used as the input in a FEM dipole model in COMSOL using an RF module. The percentage of magnetization change was determined by the previous micromagnetic model. The equivalent current of an infinitesimal magnetic dipole was first calculated and then transferred to the induced field in free

space. To obtain the received power from the receiving probe, integration was performed over the aperture area. With a certain number of magnetic strips, the power versus distance was shown in Figure 3-6. The results indicated that with a sufficient number of elements, the device could produce a detectable signal away from the device under test (DUT). The inset shows the simulated radiation pattern. The XBAR configuration does not have the same shielding effect as the BAW configuration because it lacks a complete top metallic thin film. As a result, the piezoelectric layer and wires will also radiate, which is considered a parasitic effect. The radiation pattern included contributions from a magnetic dipole, an electric dipole, and wires in the FEM model. The magnetic dipole pointed along the easy axis, while the other two pointed in the out-of-plane direction. The detailed field contribution from each component is given in Table 1. E is in V/m and H is in A/m. In the near field, the magnetic dipole's radiation dominates, as marked in red color. Far-field transformation and array transformation can also be performed in FEM.

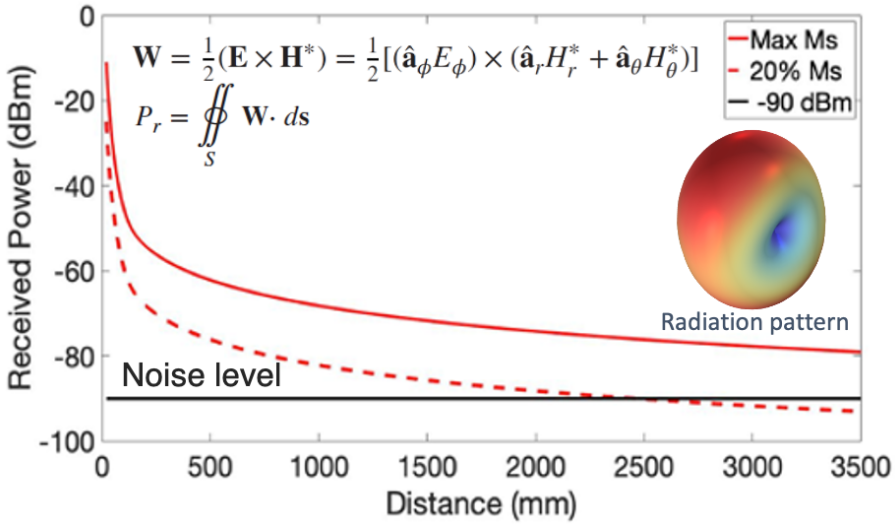

Figure 3-6: Radiation strength measured by a receiving probe and the radiation pattern.

420 MHz	E (2,0,0)	H (2,0,0)	E (0,2,0)	H (0,2,0)	E (0,0,2)	H (0,0,2)
Al wires	3.1e-4	2.1e-7	3.4e-4	2.3e-7	7.3e-4	2.2e-8
FeGaB	7.3e-3	1.1e-4	2.6e-5	*2.3e-4*	7.3e-3	1.1e-4
AlN layer	4.0e-4	1.8 e-7	3.8e-4	1.8e-7	8.1e-4	1.5e-9
All	3.8e-2	9.7e-5	4.8e-2	2.2e-4	3.3e-2	1.2e-5

Table 1: Field contributions from different components of the resonator, distance in cm.

4) Transmission line

The equivalent circuit method was used for computational efficiency. This method is based on the mathematical similarity, specifically second-order differential equations, between a mechanical resonance system and an electrical resonance system. The electromechanical parameters of piezo resonators can be extracted using the modified Butterworth-Van Dyke (MBVD) model, which simplifies the fitting process. A more sophisticated equivalent circuit for a magnetoelectric (ME) antenna is shown in Figure 3-7. This circuit is composed of a transmission line, a mechanical oscillator, and a magnetization oscillator. The transmission line is characterized by the parasitic effects of its inductance (L_f), capacitance (C_f), and resistance (R_f). The mechanical oscillator is characterized by the capacitance between the top and bottom electrodes (C_{IDT}), the electromechanical coupling transformer with turns ratio k_E^2, the mechanical stiffness (C_{mech}), the mechanical resistance (R_{mech}), and the inductor representing the energy stored in mechanical vibration. The magnetization oscillator is characterized by the magnetostrictive coupling transformer with turns ratio k_E^2, the resistance due to Gilbert damping (R_{mag}), and the resistance

due to electromagnetic (EM) radiation loss (R_{rad}). This portion of the circuit is in parallel with the LC resonance branch, as the radiation is proportional to the derivative of the current.

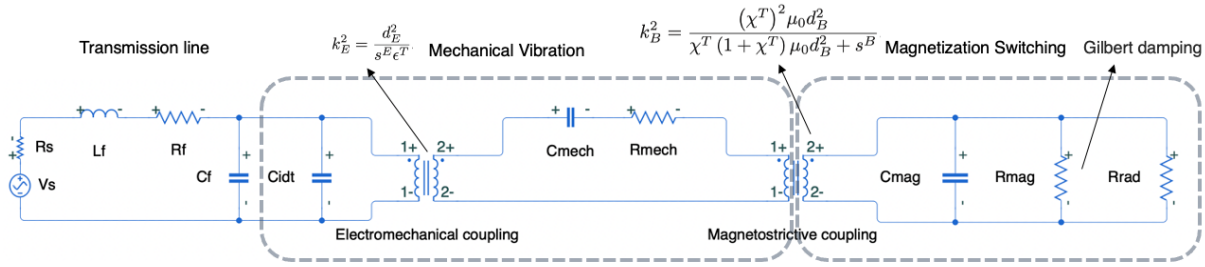

Figure 3-7: Equivalent circuit of a ME antenna.

The FEA-circuit coupled model was built using the COMSOL simulation platform. The model utilized solid mechanics, electrostatics, and electrical circuit modules to represent the resonator, and employed terminals to stimulate the system. Transmission lines were represented by idealized electrical components, and external current-terminal coupling was used to link the voltage on the piezoelectric thin film to the voltage in the circuit. This model was computationally efficient compared to fully coupled models that included piezo-elasticity and Maxwell's equations. It served as an intermediate step during the development process and produced results that were in agreement with those from the FEA model.

3.3.3 Reception mode

In reception mode, the process is largely the reverse of what was previously discussed. A FEM was built in COMSOL to include all relevant physical phenomena. The equations were solved using a segregated approach. A fully coupled solver that employed the alternating direction

implicit-finite difference time domain (ADI-FDTD) method was also considered. The model simulated the magnetostriction in FeGaB and the induced voltage in AlN under the input of a spatially uniform, sinusoidal H field in the surrounding air. Maxwell's equations were used to determine the global E and H fields. Inside the solid, the piezo-elasticity was temporally assumed to be electrostatic. An experimental measurement of the nonlinear magnetostriction curve for FeGaB was used to determine the strain. The radiation from the AlN layer and Al electrodes was neglected. Figure 3-8 shows the in-plane electric field distribution inside the AlN layer, which induced the magneto-electric (ME) voltage detected on the Al electrodes. In the frequency domain, the resonant frequency in the A0 mode showed good coherence with the transmission mode model.

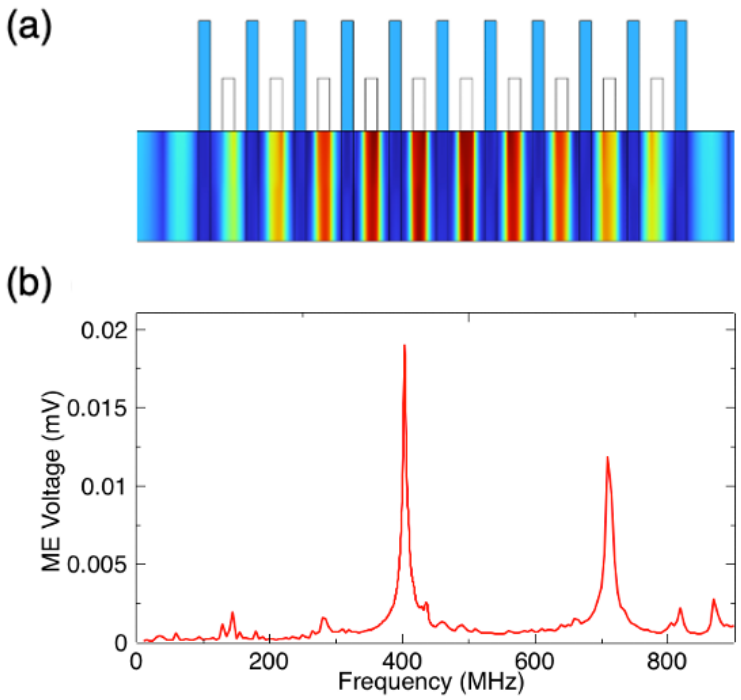

Figure 3-8： Electric field distribution and ME voltage in the frequency domain.

3.4 Fabrication

Figure 3-9 shows the characterization of the vibration sample magnetometer (VSM) and bending beam magnetostriction for FeGaB, which was deposited under a 45° bias magnetic field. The material exhibits an easy axis with a low coercivity of 1 Oe and a high saturation magnetization of 1050 emu/cc. The saturation strain reaches 60 ppm, and the piezomagnetic coefficient is 4 ppm/Oe. It is important to note that the 400 MHz XBAR ME antenna operates in the linear region for both the ferromagnetic and magnetoelastic materials.[126]

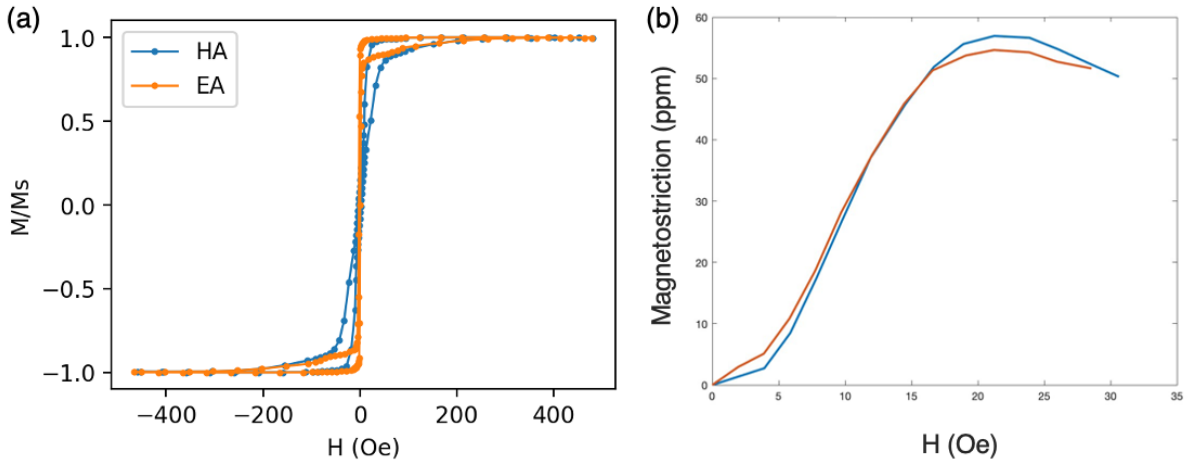

Figure 3-9: M-H curve and magnetostriction curve of FeGaB

The antenna was fabricated using microelectromechanical systems (MEMS) techniques. It consisted of four layers. The first layer was a 100-nm-thick Pt layer deposited on a 4-inch Si wafer, which served as the bottom electrode. A 1-µm-thick AlN film with residual tensile stress was then deposited as the piezoelectric material. Vias were wet-etched to expose the ground. Next, a 1-µm-thick Al layer was deposited and patterned as the top electrodes. After that, a 500-nm-thick FeGaB

film with a SiO_2 interlayer to prevent eddy currents was deposited and patterned as the ferromagnetic material. The structure included 20 magnetic bars in a single element to increase the magnetic material volume, and multiple elements could be included in a single array. The deposition was performed with a in-plane bias magnetic field at 45° in order to induce the easy axis for magnetization and align the magnetic domains. The structure was then released by a Cl_2-based inductively coupled plasma (ICP) etch to shape the hole, followed by a XeF_2 dry etch to chemically remove the Si. This allowed the resonator to vibrate freely and increase the mechanical resonance. The final device is shown in Figure 3-10. Each pattern contains lots of elements to increase the radiation signal strength. It can be measured either with wire bonding to a printed circuit board (PCB) or with a ground-signal-ground (GSG) probe on an RF probe station. The latter method is preferable as it avoids the introduction of parasitic signals by the PCB.

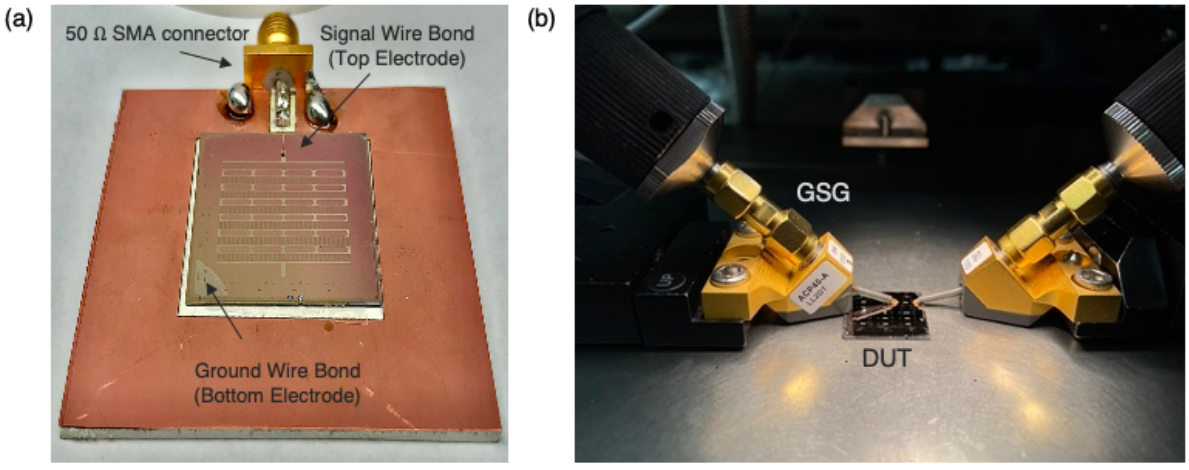

Figure 3-10: Final Device on PCB or with GSG probe.

Zoomed-in pictures of the device are shown in Figure 3-11. Single elements with different configurations were studied, and elements were also connected with a bus line to form an array for radiation measurement.

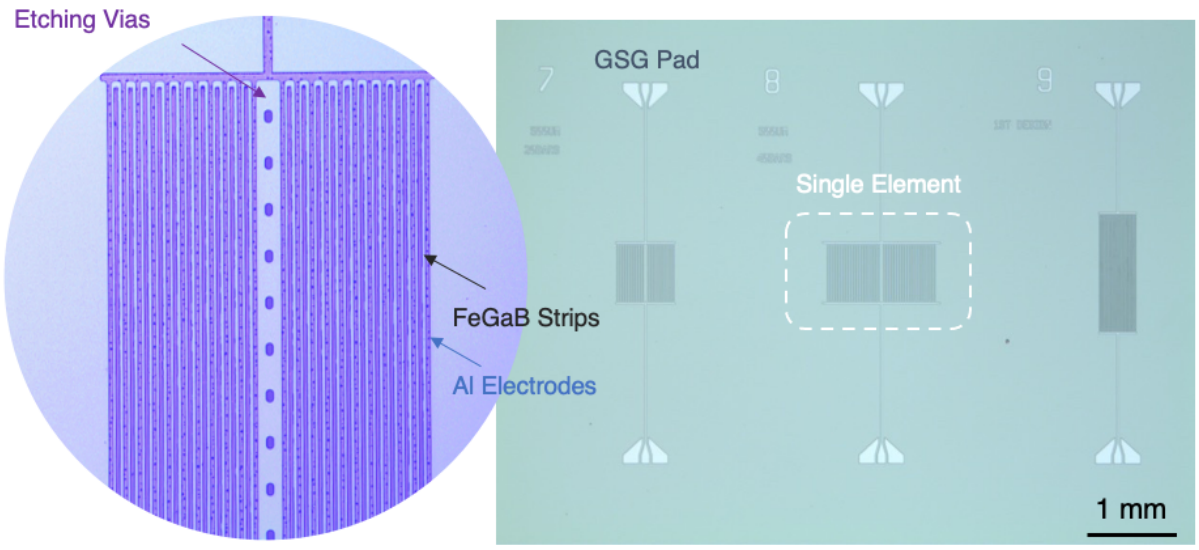

Figure 3-11: Zoom-in views of the single element with different configurations.

3.5 Results and discussion

3.5.1 Reflection coefficient S11

The reflection coefficient S11 was measured with a 10 dBm input power applied to the GSG probe. Figure 3-12 shows the mechanical resonance at 420 MHz. The frequency shift is due to the lithography inaccuracy. The curve shifts under different bias DC magnetic fields, which can be attributed to the ΔE effect [127], where the bias magnetic field modifies the FeGaB's Young's modulus. This demonstrates the magneto-electric (ME) coupling of the device.

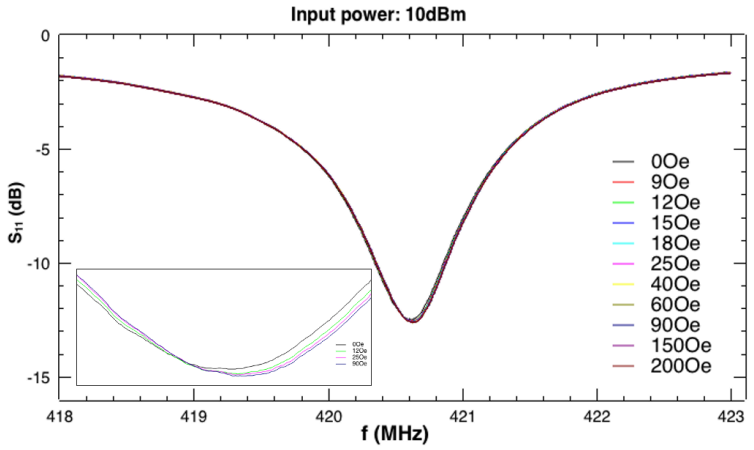

Figure 3-12: Reflection coefficient S11 of a single element under bias magnetic field.

The device was also measured with wire bonding and a PCB. The results are attached for reference. Different identical elements on the same chip were wire bonded and measured separately, as shown in Figure 3-13. The measurements exhibit good repeatability but with some variation outside the resonance frequency region. This is due to the extra impedance introduced by the wire bond, which highlights the superiority of GSG direct measurement.

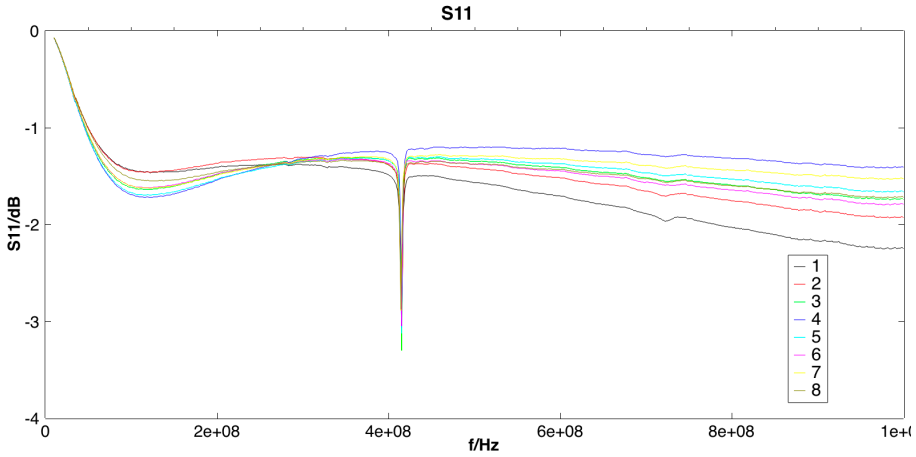

Figure 3-13: S11 from identical elements show good repeatability.

When elements were wire bonded in parallel and measured on a PCB, as shown in Figure 3-14, the increase in the number of elements caused a decrease in the mechanical resonance. This is because the impedance matching gets worse and less energy is delivered to the resonator. Ideally, a parallel and series combined connection would be used when a large number of elements are needed to increase the radiation strength. Further study is needed to design a carefully optimized array configuration.

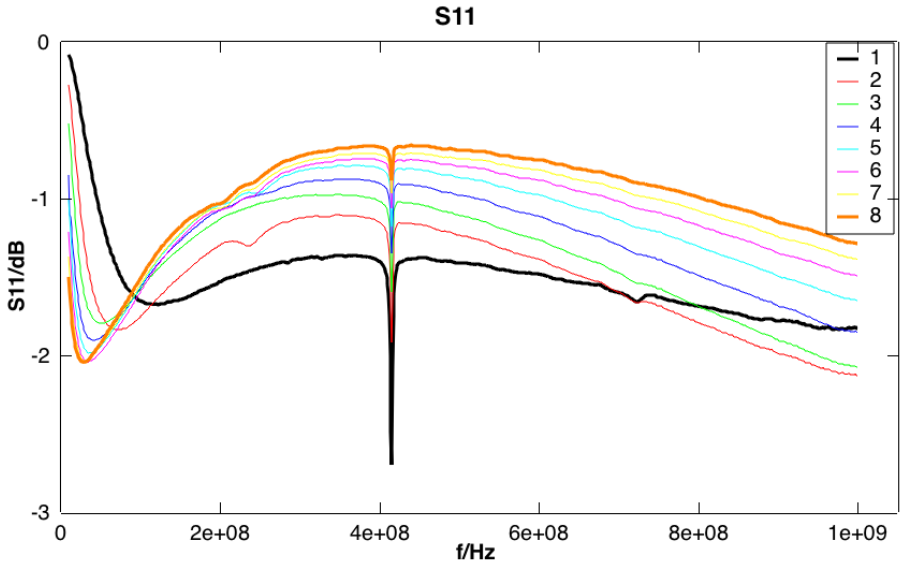

Figure 3-14: S11 with different numbers of elements connected in parallel

3.5.2 Transmission coefficient S21

The transmission coefficient S21 was measured on a probe station. Port one was connected to the GSG pad with a 30 dBm input power after amplification, while port two was connected to a magnetic probe placed on top of the device. The setup is shown in Figure 3-15.

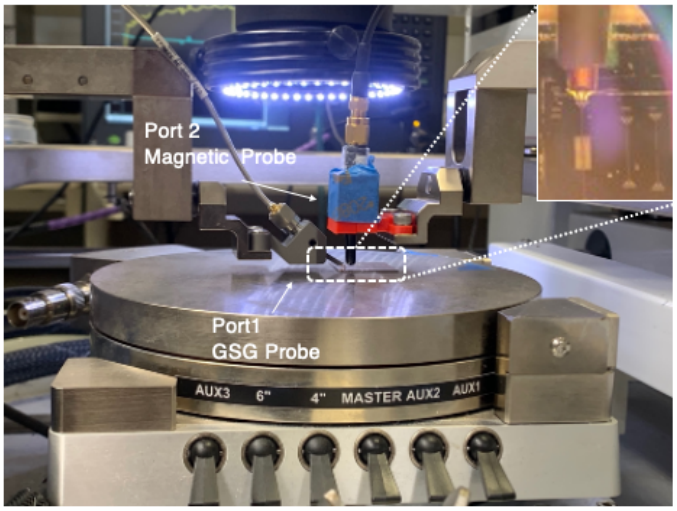

Figure 3-15: Transmission coefficient S21 measurement setup.

Figure 3-16 shows the detected magnetic field strength, which reaches a maximum at the resonance frequency. The curve shifts under different bias DC magnetic fields, which can be attributed to the ΔE effect and demonstrates the magneto-electric (ME) coupling of the device. The device shows detectable signal. But the experimental parasitic effects still need further investigation.

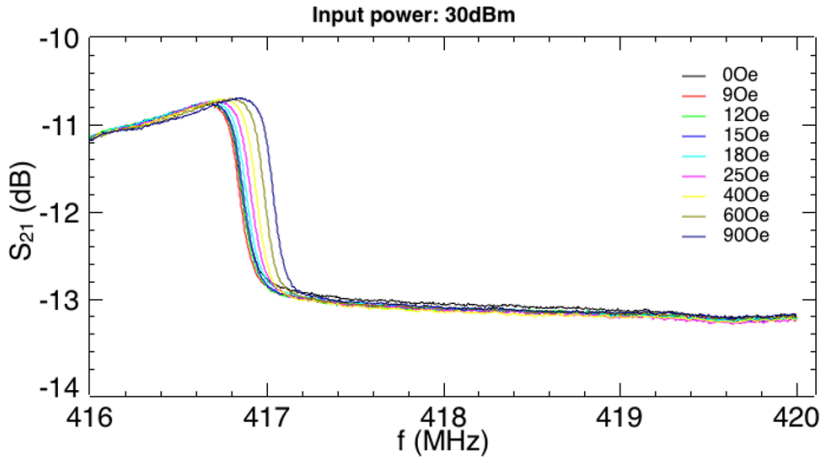

Figure 3-16: Transmission coefficient S21 of a single element under bias magnetic field.

Chapter 4. Summary

In this thesis, we present a methodology for designing microscale magnetic devices and provide details for two specific examples. We focus on utilizing the inherent magnetic energy of these devices to improve their performance.

In Chapter 1, we introduce the concept of multiferroics. By incorporating piezoelectric-magnetoelastic layers into heterostructures, we are able to achieve a magnetoelectric coupling coefficient that is several orders of magnitude higher than that of single-phase multiferroics. This allows us to more efficiently control magnetism in miniaturized devices, leading to the development of more compact and power-efficient strain-mediated magnetoelectric coupling-based applications such as data storage devices, radio-frequency devices, and microfluidic devices.

In Chapter 2, we describe the design and implementation of a micromagnetic device for single-cell manipulation. We provide a detailed account of the design process and the progress made at each step. We use stationary and dynamic models to accurately predict the magnetic forces and the trajectory of magnetic beads, respectively. Our simulations are shown to be in good agreement with experimental results. The final device successfully captures and releases magnetic beads and magnetically labeled cells using a compact array design that allows for individual control of each magnet, i.e., individual control of each captured cell.

In Chapter 3, we present a multiferroic device for its use in implantable device communication. We demonstrate a 400 MHz XBAR magnetoelectric antenna that operates at

acoustic resonance in the laterally excited standing shear bulk wave mode. This mode is more compatible with CMOS technology in the MICS band. In transmission mode, we investigate three aspects in the simulation: piezo-elasticity, micro-magnetics, and magnetic dipole radiation. We also consider the parasitic effects of the piezoelectric substrate and the wire on the model. In reception mode, we use an integrated FEM model with a segregated solver to investigate the behavior of the device. The final fabricated device successfully demonstrates mechanical resonance and magnetostrictive effects through S11 and S21 measurements. The antenna has a size of 400 × 1000 μm, which is smaller than conventional antennas by orders of magnitude, and a high Q-factor of 500. It shows promise for compact antenna design, including the possibility of improved array arrangements in order to obtain a certain radiation intensity in the future.

Overall, microscale magnetoelectric devices exhibit excellent performance in terms of bio-compatibility, miniaturization, low decay in lossy media, integrated compatibility with CMOS technology, and ground plane immunity. Although their fabrication can be challenging, these devices have a bright future in a wide range of energy-efficient technological applications. By providing examples of cell manipulation and acoustic resonators, we hope to inspire readers to explore the potential of microscale magnetic devices that go beyond traditional applications.

Reference

[1] G. Yu *et al.*, "Switching of perpendicular magnetization by spin-orbit torques in the absence of external magnetic fields.," *Nat. Nanotechnol.*, vol. 9, no. May, p. 548, 2014.

[2] Z. Diao *et al.*, "Spin-transfer torque switching in magnetic tunnel junctions and spin-transfer torque random access memory," *J. Phys. Condens. Matter*, vol. 19, no. 16, p. 165209, 2007.

[3] K. L. Wang, J. G. Alzate, and P. Khalili Amiri, "Low-power non-volatile spintronic memory: STT-RAM and beyond," *J. Phys. D. Appl. Phys.*, vol. 46, no. 7, p. 074003, 2013.

[4] A. Brataas, A. D. Kent, and H. Ohno, "Current-induced torques in magnetic materials," *Nat. Mater.*, vol. 11, no. 5, pp. 372–381, 2012.

[5] S. Fukami, T. Anekawa, C. Zhang, and H. Ohno, "A spin–orbit torque switching scheme with collinear magnetic easy axis and current configuration," *Nat. Nanotechnol.*, vol. 11, no. 7, pp. 621–625, 2016.

[6] L. Liu, C.-F. C. Pai, Y. Li, H. W. Tseng, D. C. Ralph, and R. A. Buhrman, "Spin-Torque Switching with the Giant Spin Hall Effect of Tantalum," *Science (80-.).*, vol. 336, no. May, pp. 555–559, 2012.

[7] D. Bedau *et al.*, "Ultrafast spin-transfer switching in spin valve nanopillars with perpendicular anisotropy," *Appl. Phys. Lett.*, vol. 96, no. 2, pp. 98–101, 2010.

[8] G. E. Rowlands *et al.*, "Deep subnanosecond spin torque switching in magnetic tunnel junctions with combined in-plane and perpendicular polarizers," *Appl. Phys. Lett.*, vol. 98, no. 10, 2011.

[9] Y. Shiota, T. Nozaki, F. Bonell, S. Murakami, T. Shinjo, and Y. Suzuki, "Induction of coherent magnetization switching in a few atomic layers of FeCo using voltage pulses," *Nat. Mater.*, vol. 11, no. 1, pp. 39–43, 2012.

[10] W. G. Wang, M. Li, S. Hageman, and C. L. Chien, "Electric-field-assisted switching in magnetic tunneljunctions," *Nat. Mater.*, vol. 11, no. 1, pp. 64–68, 2012.

[11] S. Kanai, M. Yamanouchi, S. Ikeda, Y. Nakatani, F. Matsukura, and H. Ohno, "Electric field-induced magnetization reversal in a perpendicular-anisotropy CoFeB-MgO magnetic tunnel junction," *Appl. Phys. Lett.*, vol. 101, no. 12, pp. 2010–2013, 2012.

[12] Y. H. Chu, L. W. Martin, M. B. Holcomb, and R. Ramesh, "Controlling magnetism with multiferroics," *Mater. Today*, vol. 10, no. 10, pp. 16–23, 2007.

[13] L. W. Martin, S. P. Crane, C. A. F. Vaz, D. Sando, and M. Bibes, "Spintronics with multiferroics," vol. 3, 2008.

[14] B. G. Catalan and J. F. Scott, "Physics and Applications of Bismuth Ferrite," pp. 2463–2485, 2009.

[15] K. F. Wang, J. Liu, and Z. F. Ren, "Advances in Physics Multiferroicity : the coupling between magnetic and polarization orders," vol. 8732, no. November, 2017.

[16] J. T. Heron, “Electric Field Control of Ferromagnetism and Magnetic Devices Using Multiferroics,” University of California, Berkeley, 2013.

[17] Y. LU, “ELECTRICAL CONTROL OF FERROMAGNETISM IN MULTIFERROIC BISMUTH FERRITE-BASED HETEROSTRUCTURES,” Nanyang Technological University, 2011.

[18] N. A. Spaldin and M. Fiebig, “The Renaissance of Magnetoelectric Multiferroics,” vol. 309, no. July, pp. 391–393, 2005.

[19] W. Eerenstein, N. D. Mathur, and J. F. Scott, “Multiferroic and magnetoelectric materials,” *Nature*, vol. 442, pp. 759–765, Aug. 2006.

[20] T. Maruyama *et al.*, “Large voltage-induced magnetic anisotropy change in a few atomic layers of iron,” *Nat. Nanotechnol.*, vol. 4, no. 3, pp. 158–161, 2009.

[21] R. Ramesh and N. A. Spaldin, “Multiferroics: progress and prospects in thin films,” *Nat. Mater.*, vol. 6, no. 1, pp. 21–29, 2007.

[22] J. Wang *et al.*, “Epitaxial BiFeO3 multiferroic thin film heterostructures,” *Science (80-.).*, vol. 299, no. 5613, pp. 1719–1722, Mar. 2003.

[23] H. Palneedi, V. Annapureddy, S. Priya, and J. Ryu, “Status and perspectives of multiferroic magnetoelectric composite materials and applications,” in *Actuators*, 2016, vol. 5, no. 1, p. 9.

[24] J. Ma *et al.*, “Recent Progress in Multiferroic Magnetoelectric Composites: from Bulk to Thin Films,” *Adv. Mater.*, vol. 23, no. 9, pp. 1062–1087, Mar. 2011.

[25] H. Uršič, M. Santo Zarnik, and M. Kosec, “ Pb(Mg 1/3 Nb 2/3)O 3 –PbTiO 3 (PMN-PT) Material for Actuator Applications ,” *Smart Mater. Res.*, vol. 2011, pp. 1–6, 2011.

[26] P. Duran and C. Moure, “Piezoelectric ceramics,” *Mater. Chem. Phys.*, vol. 15, no. 3–4, pp. 193–211, 1986.

[27] M. Acosta *et al.*, “BaTiO3-based piezoelectrics: Fundamentals, current status, and perspectives,” *Appl. Phys. Rev.*, vol. 4, no. 4, 2017.

[28] T. Wu *et al.*, “Domain engineered switchable strain states in ferroelectric (011) [Pb(Mg1/3Nb2/3)O3](1-x)-[PbTiO 3]x (PMN-PT, x≈0.32) single crystals,” *J. Appl. Phys.*, vol. 109, no. 12, pp. 0–8, 2011.

[29] J. J. Yang *et al.*, “Electric field manipulation of magnetization at room temperature in multiferroic CoFe2O4/Pb(Mg1/3Nb 2/3)0.7 Ti0.3O3 heterostructures,” *Appl. Phys. Lett.*, vol. 94, no. 21, pp. 1–4, 2009.

[30] Y. Ba *et al.*, “Spatially Resolved Electric-Field Manipulation of Magnetism for CoFeB Mesoscopic Discs on Ferroelectrics,” *Adv. Funct. Mater.*, vol. 28, no. 11, pp. 1–10, 2018.

[31] J. M. Hu *et al.*, “Purely electric-field-driven perpendicular magnetization reversal,” *Nano Lett.*, vol. 15, no. 1, pp. 616–622, 2015.

[32] R.-C. Peng, J.-M. Hu, K. Momeni, J.-J. Wang, L.-Q. Chen, and C.-W. Nan, "Fast 180° magnetization switching in a strain-mediated multiferroic heterostructure driven by a voltage," *Sci. Rep.*, vol. 6, no. 1, p. 27561, 2016.

[33] E. Rapoport and G. S. D. Beach, "Dynamics of superparamagnetic microbead transport along magnetic nanotracks by magnetic domain walls," *Appl. Phys. Lett.*, vol. 100, no. 8, 2012.

[34] C. Y. Liang *et al.*, "Electrical control of a single magnetoelastic domain structure on a clamped piezoelectric thin film - Analysis," *J. Appl. Phys.*, vol. 116, no. 12, 2014.

[35] C.-Y. Y. Liang *et al.*, "Modeling of magnetoelastic nanostructures with a fully coupled mechanical-micromagnetic model.," *Nanotechnology*, vol. 25, no. 43, p. 435701, 2014.

[36] N. A. Spaldin and R. Ramesh, "Advances in magnetoelectric multiferroics," vol. 18, no. 3, pp. 203–212, Feb. 2019.

[37] M. Bibes, "Multiferroics-Towards-a-magnetoelectric-memory," *Nat. Mater.*, vol. 7, no. June, pp. 7–8, 2008.

[38] S. Manipatruni, D. E. Nikonov, and I. A. Young, "Beyond CMOS computing with spin and polarization," *Nat. Phys.*, vol. 14, no. 4, pp. 338–343, 2018.

[39] A. A. Bukharaev, A. K. Zvezdin, A. P. Pyatakov, and Y. K. Fetisov, "Straintronics: a new trend in micro- and nanoelectronics and material science," *Uspekhi Fiz. Nauk*, vol. 188, no. 12, pp. 1288–1330, 2018.

[40] W. Peng, B. Howe, and X. Yang, “Multiferroic RF / Microwave Devices 5 . 1 Voltage Control of FMR,” 2019.

[41] A. B. Ustinov *et al.*, “Dynamic electromagnonic crystal based on artificial multiferroic heterostructure,” *Commun. Phys.*, vol. 2, no. 1, pp. 1–7, 2019.

[42] Y. C. Hsiao *et al.*, “Capturing Magnetic Bead-based Arrays Using Perpendicular Magnetic Anisotropy (PMA),” *Appl. Phys. Lett.*, vol. 115, no. 8, pp. 2–11, 2019.

[43] Z. Xiao *et al.*, “Cytocompatible magnetostrictive microstructures for nano- and microparticle manipulation on linear strain response piezoelectrics,” *Multifunct. Mater.*, vol. 1, no. 1, p. 014004, 2018.

[44] R. Acevedo, C. Y. Liang, G. P. Carman, and A. E. Sepulveda, “A decomposition approach to the design of a multiferroic memory bit,” *Front. Mech. Eng.*, vol. 12, no. 2, pp. 215–223, 2017.

[45] J. Couzin-Frankel, “Cancer immunotherapy,” *Science (80-.).*, vol. 342, no. 6165, pp. 1432–1433, 2013.

[46] J. D. Adams, U. Kim, and H. T. Soh, “Multitarget magnetic activated cell sorter,” *Proc. Natl. Acad. Sci.*, vol. 105, no. 47, pp. 18165–18170, 2008.

[47] N. Xia *et al.*, “Combined microfluidic-micromagnetic separation of living cells in continuous flow,” *Biomed. Microdevices*, vol. 8, no. 4, pp. 299–308, 2006.

[48] P. Hu, W. Zhang, H. Xin, and G. Deng, "Single cell isolation and analysis," *Front. Cell Dev. Biol.*, vol. 4, no. OCT, pp. 1–12, 2016.

[49] M. M. Wang *et al.*, "Microfluidic sorting of mammalian cells by optical force switching," *Nat. Biotechnol.*, vol. 23, no. 1, pp. 83–87, 2005.

[50] Z. T. F. Yu, K. M. Aw Yong, and J. Fu, "Microfluidic blood cell sorting: Now and beyond," *Small*, vol. 10, no. 9, pp. 1687–1703, 2014.

[51] A. A. S. Bhagat, H. Bow, H. W. Hou, S. J. Tan, J. Han, and C. T. Lim, "Microfluidics for cell separation," *Med. Biol. Eng. Comput.*, vol. 48, no. 10, pp. 999–1014, 2010.

[52] C. Wyatt Shields Iv, C. D. Reyes, and G. P. López, "Microfluidic cell sorting: A review of the advances in the separation of cells from debulking to rare cell isolation," *Lab Chip*, vol. 15, no. 5, pp. 1230–1249, Mar. 2015.

[53] M. Berger, J. Castelino, R. Huang, M. Shah, and R. H. Austin, "Design of a microfabricated magnetic cell separator," *Electrophoresis*, vol. 22, no. 18, pp. 3883–3892, 2001.

[54] S. Miltenyi, W. Müller, W. Weichel, and A. Radbruch, "High gradient magnetic cell separation with MACS," *Cytometry*, vol. 11, no. 2, pp. 231–238, 1990.

[55] A. E. Saliba *et al.*, "Microfluidic sorting and multimodal typing of cancer cells in self-assembled magnetic arrays," *Proc. Natl. Acad. Sci. U. S. A.*, vol. 107, no. 33, pp. 14524–14529, 2010.

[56] K. Hoshino *et al.*, "Microchip-based immunomagnetic detection of circulating tumor cells," *Lab Chip*, vol. 11, no. 20, pp. 3449–3457, 2011.

[57] E. Ozkumur *et al.*, "Inertial focusing for tumor antigen-dependent and -independent sorting of rare circulating tumor cells," *Sci. Transl. Med.*, vol. 5, no. 179, 2013.

[58] J. Nam, H. Huang, H. Lim, C. Lim, and S. Shin, "Magnetic separation of malaria-infected red blood cells in various developmental stages," *Anal. Chem.*, vol. 85, no. 15, pp. 7316–7323, 2013.

[59] R. T. Krivacic *et al.*, "A rare-cell detector for cancer," *Proc. Natl. Acad. Sci. U. S. A.*, vol. 101, no. 29, pp. 10501–10504, 2004.

[60] J. C. Baret *et al.*, "Fluorescence-activated droplet sorting (FADS): Efficient microfluidic cell sorting based on enzymatic activity," *Lab Chip*, vol. 9, no. 13, pp. 1850–1858, 2009.

[61] O. D. Velev and K. H. Bhatt, "On-chip micromanipulation and assembly of colloidal particles by electric fields," *Soft Matter*, vol. 2, no. 9, pp. 738–750, 2006.

[62] C. T. Ho, R. Z. Lin, W. Y. Chang, H. Y. Chang, and C. H. Liu, "Rapid heterogeneous liver-cell on-chip patterning via the enhanced field-induced dielectrophoresis trap," *Lab Chip*, vol. 6, no. 6, pp. 724–734, 2006.

[63] X. Ding *et al.*, "Standing surface acoustic wave (SSAW) based multichannel cell sorting," *Lab Chip*, vol. 12, no. 21, pp. 4228–4231, 2012.

[64] D. Di Carlo, J. F. Edd, D. Irimia, R. G. Tompkins, and M. Toner, "Equilibrium separation and filtration of particles using differential inertial focusing," *Anal. Chem.*, vol. 80, no. 6, pp. 2204–2211, 2008.

[65] M. Donolato *et al.*, "On-chip manipulation of protein-coated magnetic beads via domain-wall conduits," *Adv. Mater.*, vol. 22, no. 24, pp. 2706–2710, 2010.

[66] E. Rapoport and G. S. D. Beach, "Magneto-mechanical resonance of a single superparamagnetic microbead trapped by a magnetic domain wall," *J. Appl. Phys.*, vol. 111, no. 7, pp. 1–4, 2012.

[67] E. Rapoport and G. S. D. Beach, "Transport dynamics of superparamagnetic microbeads trapped by mobile magnetic domain walls," *Phys. Rev. B - Condens. Matter Mater. Phys.*, vol. 87, no. 17, pp. 21–24, 2013.

[68] U. Bauer, S. Emori, and G. S. D. Beach, "Voltage-controlled domain wall traps in ferromagnetic nanowires," *Nat. Nanotechnol.*, vol. 8, no. 6, pp. 411–416, 2013.

[69] A. Sarella, A. Torti, M. Donolato, M. Pancaldi, and P. Vavassori, "Two-dimensional programmable manipulation of magnetic nanoparticles on-chip," *Adv. Mater.*, vol. 26, no. 15, pp. 2384–2390, 2014.

[70] A. Tay, C. Murray, and D. Di Carlo, "Phenotypic Selection of Magnetospirillum magneticum (AMB-1) Overproducers Using Magnetic Ratcheting," *Adv. Funct. Mater.*, vol. 27, no. 41, pp. 1–8, 2017.

[71] W. Yu *et al.*, "A ferrobotic system for automated microfluidic logistics," *Sci. Robot.*, vol. 5, no. 39, pp. 1–12, 2020.

[72] H. Lin *et al.*, "Ferrobotic swarms enable accessible and adaptable automated viral testing," *Nature*, vol. 611, no. March, 2022.

[73] M. Niemier *et al.*, "Clocking structures and power analysis for nanomagnet-based logic devices," *Proc. Int. Symp. Low Power Electron. Des.*, pp. 26–31, 2007.

[74] H. Sohn *et al.*, "Electrically driven magnetic domain wall rotation in multiferroic heterostructures to manipulate suspended on-chip magnetic particles," *ACS Nano*, vol. 9, no. 5, pp. 4814–4826, 2015.

[75] H. Sohn *et al.*, "Deterministic multi-step rotation of magnetic single-domain state in Nickel nanodisks using multiferroic magnetoelastic coupling," *J. Magn. Magn. Mater.*, vol. 439, pp. 196–202, 2017.

[76] R. Khojah *et al.*, "Single-Domain Multiferroic Array-Addressable Terfenol-D (SMArT) Micromagnets for Programmable Single-Cell Capture and Release," *Adv. Mater.*, vol. 33, no. 20, pp. 1–8, 2021.

[77] S. Ikeda *et al.*, "A perpendicular-anisotropy CoFeB–MgO magnetic tunnel junction," *Nat. Mater.*, vol. 9, no. 9, pp. 721–724, 2010.

[78] R.-C. Peng, J.-M. Hu, L.-Q. Chen, and C.-W. Nan, "On the speed of piezostrain-mediated voltage-driven perpendicular magnetization reversal: a computational elastodynamics-

micromagnetic phase-field study," *NPG Asia Mater.*, vol. 9, no. 7, p. e404, 2017.

[79] X. Li *et al.*, "Strain-mediated 180° perpendicular magnetization switching of a single domain multiferroic structure," *J. Appl. Phys.*, vol. 118, no. 1, 2015.

[80] Q. Wang *et al.*, "Strain-mediated 180° switching in CoFeB and Terfenol-D nanodots with perpendicular magnetic anisotropy," *Appl. Phys. Lett.*, vol. 110, no. 10, pp. 1–6, 2017.

[81] P. Gambardella and I. M. Miron, "Current-induced spin-orbit torques," *Philos. Trans. R. Soc. A Math. Phys. Eng. Sci.*, vol. 369, no. 1948, pp. 3175–3197, 2011.

[82] W. Y. Kwak, J. H. Kwon, P. Grünberg, S. H. Han, and B. K. Cho, "Current-induced magnetic switching with spin-orbit torque in an interlayer-coupled junction with a Ta spacer layer," *Sci. Rep.*, vol. 8, no. 1, pp. 1–7, 2018.

[83] S. Fukami, C. Zhang, S. Duttagupta, A. Kurenkov, and H. Ohno, "Magnetization switching by spin-orbit torque in an antiferromagnet-ferromagnet bilayer system," *Nat. Mater.*, vol. 15, no. 5, pp. 535–541, 2016.

[84] Y. Fan *et al.*, "Magnetization switching through giant spin-orbit torque in a magnetically doped topological insulator heterostructure," *Nat. Mater.*, vol. 13, no. 7, pp. 699–704, 2014.

[85] M. H. Nguyen, D. C. Ralph, and R. A. Buhrman, "Spin Torque Study of the Spin Hall Conductivity and Spin Diffusion Length in Platinum Thin Films with Varying Resistivity," *Phys. Rev. Lett.*, vol. 116, no. 12, pp. 1–6, 2016.

[86] D. C. Worledge *et al.*, "Spin torque switching of perpendicular Ta|CoFeB|MgO-based magnetic tunnel junctions," *Appl. Phys. Lett.*, vol. 98, no. 2, pp. 93–96, 2011.

[87] S. Sharma, V. K. Katiyar, and U. Singh, "Mathematical modelling for trajectories of magnetic nanoparticles in a blood vessel under magnetic field," *J. Magn. Magn. Mater.*, vol. 379, pp. 102–107, 2015.

[88] Q. Cao, X. Han, and L. Li, "Numerical analysis of magnetic nanoparticle transport in microfluidic systems under the influence of permanent magnets," *J. Phys. D. Appl. Phys.*, vol. 45, no. 46, 2012.

[89] S. S. Shevkoplyas, A. C. Siegel, R. M. Westervelt, M. G. Prentiss, and G. M. Whitesides, "The force acting on a superparamagnetic bead due to an applied magnetic field," *Lab Chip*, vol. 7, no. 10, pp. 1294–1302, 2007.

[90] O. Karaagac and H. Kockar, "A simple way to obtain high saturation magnetization for superparamagnetic iron oxide nanoparticles synthesized in air atmosphere: Optimization by experimental design," *J. Magn. Magn. Mater.*, vol. 409, pp. 116–123, 2016.

[91] S. Veintemillas-Verdaguer *et al.*, "Colloidal dispersions of maghemite nanoparticles produced by laser pyrolysis with application as NMR contrast agents," *J. Phys. D. Appl. Phys.*, vol. 37, no. 15, pp. 2054–2059, 2004.

[92] N. Pamme, "Magnetism and microfluidics," vol. 1, 2006.

[93] B. Anghinoni, G. A. S. Flizikowski, L. C. Malacarne, M. Partanen, S. E. Bialkowski, and

N. G. C. Astrath, “On the formulations of the electromagnetic stress–energy tensor,” *Ann. Phys. (N. Y).*, vol. 443, p. 169004, 2022.

[94] S. Wang, Y. Zhou, J. Tan, J. Xu, J. Yang, and Y. Liu, “Computational modeling of magnetic nanoparticle targeting to stent surface under high gradient field,” *Comput. Mech.*, vol. 53, no. 3, pp. 403–412, 2014.

[95] S. Perhirin and Y. Auffret, “AN EFFICIENT METAMATERIAL- INSPIRED ELECTRICALLY-SMALL ANTENNA,” *Microw. Opt. Technol. Lett.*, vol. 55, no. 11, pp. 2562–2568, 2013.

[96] E. G. Turitsyna and S. Webb, “Design of thin, efficient, electrically small antenna using multiple foldings,” *Electron. Lett.*, vol. 41, no. 2, pp. 40–41, 2005.

[97] R. W. Ziolkowski, “An efficient, electrically small antenna designed for VHF and UHF applications,” *IEEE Antennas Wirel. Propag. Lett.*, vol. 7, pp. 217–220, 2008.

[98] M. A. Kemp *et al.*, “A high Q piezoelectric resonator as a portable VLF transmitter,” *Nat. Commun.*, vol. 10, no. 1, pp. 1–7, 2019.

[99] J. Xu *et al.*, “A low frequency mechanical transmitter based on magnetoelectric heterostructures operated at their resonance frequency,” *Sensors (Switzerland)*, vol. 19, no. 4, 2019.

[100] J. D. Schneider *et al.*, “Experimental demonstration and operating principles of a multiferroic antenna,” *J. Appl. Phys.*, vol. 126, no. 22, 2019.

[101] J. A. Bickford, R. S. Mcnabb, P. A. Ward, D. K. Freeman, and M. S. Weinberg, “Low Frequency Mechanical Antennas,” *2017 IEEE Int. Symp. Antennas Propag. Usn. Natl. Radio Sci. Meet.*, pp. 1475–1476, 2017.

[102] M. N. Srinivas Prasad, F. Fereidoony, and Y. E. Wang, “2D Stacked Magnetic Pendulum Arrays for Efficient ULF Transmission,” *2020 IEEE Int. Symp. Antennas Propag. North Am. Radio Sci. Meet. IEEECONF 2020 - Proc.*, pp. 1305–1306, 2020.

[103] Z. Yao, Y. E. Wang, S. Keller, and G. P. Carman, “Bulk Acoustic Wave-Mediated Multiferroic Antennas: Architecture and Performance Bound,” *IEEE Trans. Antennas Propag.*, vol. 63, no. 8, pp. 3335–3344, 2015.

[104] Z. Chu *et al.*, “A low-power and high-sensitivity magnetic field sensor based on converse magnetoelectric effect,” *Appl. Phys. Lett.*, vol. 115, no. 16, 2019.

[105] C. Dong *et al.*, “A Portable Very Low Frequency (VLF) Communication System Based on Acoustically Actuated Magnetoelectric Antennas,” *IEEE Antennas Wirel. Propag. Lett.*, vol. 19, no. 3, pp. 398–402, 2020.

[106] H. Lin *et al.*, “Future Antenna Miniaturization Mechanism: Magnetoelectric Antennas,” *IEEE MTT-S Int. Microw. Symp. Dig.*, vol. 2018-June, pp. 220–223, 2018.

[107] P. J. Shah, D. A. Bas, I. Lisenkov, A. Matyushov, N. X. Sun, and M. R. Page, “Giant nonreciprocity of surface acoustic waves enabled by the magnetoelastic interaction,” *Sci. Adv.*, vol. 6, no. 49, pp. 2–8, 2020.

[108] H. Chen *et al.*, “Integrated Tunable Magnetoelectric RF Inductors,” *IEEE Trans. Microw. Theory Tech.*, vol. 68, no. 3, pp. 951–963, 2020.

[109] M. Nasrollahpour *et al.*, “Integration of a novel CMOS-compatible magnetoelectric antenna with a low-noise amplifier and a tunable input matching,” *Analog Integr. Circuits Signal Process.*, vol. 105, no. 3, pp. 407–415, 2020.

[110] X. Liang, H. Chen, and N. X. Sun, “Magnetoelectric materials and devices,” *APL Mater.*, vol. 9, no. 4, 2021.

[111] C. Tu *et al.*, “Mechanical-resonance-enhanced thin-film magnetoelectric heterostructures for magnetometers, mechanical antennas, tunable RF inductors, and filters,” *Materials (Basel).*, vol. 12, no. 14, 2019.

[112] M. Zaeimbashi *et al.*, “NanoNeuroRFID: A Wireless Implantable Device Based on Magnetoelectric Antennas,” *IEEE J. Electromagn. RF Microwaves Med. Biol.*, vol. 3, no. 3, pp. 206–215, 2019.

[113] J. Lou, R. E. Insignares, Z. Cai, K. S. Ziemer, M. Liu, and N. X. Sun, “Soft magnetism, magnetostriction, and microwave properties of FeGaB thin films,” *Appl. Phys. Lett.*, vol. 91, no. 18, pp. 18–20, 2007.

[114] M. Zaeimbashi *et al.*, “Ultra-compact dual-band smart NEMS magnetoelectric antennas for simultaneous wireless energy harvesting and magnetic field sensing,” *Nat. Commun.*, vol. 12, no. 1, 2021.

[115] M. Li *et al.*, "Ultra-sensitive NEMS magnetoelectric sensor for picotesla DC magnetic field detection," *Appl. Phys. Lett.*, vol. 110, no. 14, 2017.

[116] A. E. Hassanien, M. Breen, M. H. Li, and S. Gong, "Acoustically driven electromagnetic radiating elements," *Sci. Rep.*, vol. 10, no. 1, pp. 1–12, 2020.

[117] J. D. Schneider *et al.*, "Frequency conversion through nonlinear mixing in acoustic waves," *J. Appl. Phys.*, vol. 128, no. 6, 2020.

[118] Z. Yao *et al.*, "Modeling of Multiple Dynamics in the Radiation of Bulk Acoustic Wave Antennas," *IEEE J. Multiscale Multiphysics Comput. Tech.*, vol. 5, pp. 7–20, 2020.

[119] L. Arapan, I. Katardjiev, and V. Yantchev, "An intermode-coupled thin-film micro-acoustic resonator," *J. Micromechanics Microengineering*, vol. 22, no. 8, 2012.

[120] Y. Liu, Y. Cai, Y. Zhang, A. Tovstopyat, S. Liu, and C. Sun, "Materials, design, and characteristics of bulk acoustic wave resonator: A review," *Micromachines*, vol. 11, no. 7, 2020.

[121] S. Yandrapalli, V. Plessky, J. Koskela, V. Yantchev, P. Turner, and L. G. Villanueva, "Analysis of XBAR resonance and higher order spurious modes," *IEEE Int. Ultrason. Symp. IUS*, vol. 2019-Octob, pp. 185–188, 2019.

[122] V. Yantchev and I. Katardjiev, "Thin film Lamb wave resonators in frequency control and sensing applications: A review," *J. Micromechanics Microengineering*, vol. 23, no. 4, 2013.

[123] T. Nan *et al.*, “Acoustically actuated ultra-compact NEMS magnetoelectric antennas,” *Nat. Commun.*, vol. 8, no. 1, pp. 1–7, 2017.

[124] C. Willberg, S. Duczek, J. M. Vivar Perez, D. Schmicker, and U. Gabbert, “Comparison of different higher order finite element schemes for the simulation of Lamb waves,” *Comput. Methods Appl. Mech. Eng.*, vol. 241–244, pp. 246–261, 2012.

[125] Y. K. Yong, M. Patel, J. Vig, and A. Ballato, “Effects of electromagnetic radiation on the Q of quartz resonators,” *IEEE Trans. Ultrason. Ferroelectr. Freq. Control*, vol. 56, no. 2, pp. 353–360, 2009.

[126] C. Dong *et al.*, “Characterization of magnetomechanical properties in FeGaB thin films,” *Appl. Phys. Lett.*, vol. 113, no. 26, 2018.

[127] T. Nan, Y. Hui, M. Rinaldi, and N. X. Sun, “Self-biased 215MHz magnetoelectric NEMS resonator for ultra-sensitive DC magnetic field detection,” *Sci. Rep.*, vol. 3, pp. 1–6, 2013.